

CALCULATION OF FISSION BARRIERS

by

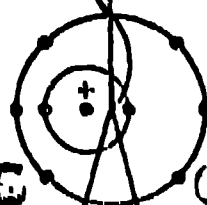
P. Möller and J. R. Nix

August 1, 1973

For presentation at the Third IAEA Symposium on the  
Physics and Chemistry of Fission  
Rochester, New York, August 13-17, 1973

By acceptance of this article for publication, the publisher recognizes the Government's (licensor) rights in any copyright and the Government and its authorized representatives have unrestricted right to reproduce in whole or in part said article under any copyright secured by the publisher.

The Los Alamos Scientific Laboratory requests that the publisher identify this article as work performed under the auspices of the U. S. Atomic Energy Commission.

  
**Los Alamos**  
**Scientific Laboratory**  
of the University of California  
LOS ALAMOS, NEW MEXICO 87544

**NOTICE**

This report was prepared as an account of work sponsored by the United States Government. Neither the United States nor the United States Atomic Energy Commission, nor any of their employees, nor any of their contractors, subcontractors, or their employees, makes any warranty, express or implied, or assumes any legal liability or responsibility for the accuracy, completeness or usefulness of any information, apparatus, product or process disclosed, or represents that its use would not infringe privately owned rights.

**MASTER**

## CALCULATION OF FISSION BARRIERS\*

P. MÖLLER and J. R. NIX

Los Alamos Scientific Laboratory, University of California  
Los Alamos, New Mexico, United States of America

### ABSTRACT

We review recent advances in the calculation of the nuclear potential energy of deformation, including both selfconsistent microscopic methods and the macroscopic-microscopic method. Particular attention is paid to the steps that are involved in calculating the potential energy according to the latter method. These steps include specifying the nuclear shape, calculating the macroscopic (liquid-drop) energy, generating the single-particle potential, solving the Schrödinger equation, and calculating the microscopic (shell and pairing) corrections.

In the second part of the paper we present and compare the results of two new calculations that we have performed recently at Los Alamos. In the first calculation, the nuclear shapes are specified in terms of smoothly joined portions of three quadratic surfaces of revolution, which permits us to calculate the potential energy all the way to the scission point. The extrema in the potential-energy surfaces are determined by varying independently three of the coordinates in this parametrization; the ground-state energy is determined also by use of an alternative parametrization. The macroscopic energy is calculated from the droplet model of Myers and Swiatecki, which includes higher-order terms in  $A^{-1/3}$  and in  $[(N-Z)/A]^2$  than are retained in the liquid-drop model. The microscopic shell and pairing corrections are calculated by means of Strutinsky's method from the single-particle levels of a diffuse-surface folded Yukawa single-particle potential. We use a new set of potential parameters obtained from adjustments to experimental single-particle levels in heavy deformed nuclei and from statistical calculations. The second new calculation is performed with the modified oscillator potential and is similar to a previous calculation with this potential except that we now use the droplet model in place of the liquid-drop model.

These and earlier calculations provide an understanding and unification of many varied phenomena associated with nuclear shape changes: nuclear

\* This work was supported by the U. S. Atomic Energy Commission and the Swedish Atomic Research Council.

ground-state masses and deformations, second minima in the fission barriers of actinide nuclei, fission-barrier heights, and fission-fragment mass distributions. For the lighter actinide nuclei the asymmetric second saddle point is split into two individual saddle points separated by an asymmetric third minimum, which possibly resolves the thorium anomaly. The calculated energies of the local minima and saddle points in the potential-energy surfaces reproduce the experimental values to within an accuracy of about 1 MeV, although larger systematic errors are still present in some cases. The calculated properties of the saddle points also reproduce qualitatively the main features of experimental fission-fragment mass distributions.

## 1. INTRODUCTION

You probably have followed the renaissance that has taken place in our understanding of fission since the first IAEA fission symposium in Salzburg eight years ago. At that symposium we still thought that the fission barrier of a nucleus was a monotonically increasing function of deformation until it reached its maximum value and then a monotonically decreasing function of deformation. But it soon became clear that instead of this smooth behavior the fission barrier contains large fluctuations as a function of both nuclear shape and particle numbers. For some nuclei, these fluctuations lead to a fission barrier that contains two peaks separated by a second minimum, as illustrated in Fig. 1 for  $^{240}\text{Pu}$ .

By the time of the second IAEA fission symposium in Vienna four years ago, we were able to calculate such a barrier for symmetric deformations in terms of nonuniformities in the single-particle levels near the Fermi surface. We could also understand three new experimental discoveries--spontaneously fissioning isomers, broad resonances in fission cross sections, and narrow intermediate structure in fission cross sections--in terms of this second minimum.

But three major puzzles remained. First, for most actinide nuclei the calculated height of either the first peak or the second peak was several MeV higher than the experimental value. Second, the calculated fission barriers were all stable with respect to mass-asymmetric deformations, which violated the well-established preference of heavy nuclei to divide asymmetrically at low excitation energy. And third, the calculated heights of the first peak and second minimum for isotopes of thorium were substantially lower than the experimental values.

Since Vienna two of these puzzles have largely disappeared. We now know that in most actinide nuclei the second peak is unstable with respect to mass asymmetry and that in the heavier actinide nuclei the first peak is unstable with respect to axial asymmetry (gamma deformations). Instabilities of this type lower the calculated barrier heights and also provide a mechanism for an asymmetric mass division. These instabilities arise because of single-particle effects similar to those responsible for a deformed ground-state minimum and second minimum in the fission barrier. The third puzzle is not definitely solved, but we suggest later a possible resolution in terms of single-particle effects near the asymmetric second saddle point.

Our plan is first to review the various approaches that are taken in the calculation of fission barriers and second to present some new results that we have obtained at Los Alamos. We do not have space here to review

everyone's contributions but instead concentrate on recent results that best illustrate the physical principles involved. Exhaustive references to other work, as well as to the mathematical details, can be found in four recent review articles [2-5]. We then compare the calculated energies of the local minima and saddle points in the barriers with experimental results, some of which are described in this symposium by Britt, Vandenbosch, and others [6,7]. We also discuss the extent to which experimental fission-fragment mass distributions can be understood in terms of the calculated properties of the saddle-point shapes. We conclude with an assessment of our present ability to calculate fission barriers.

## 2. SELFCONSISTENT MICROSCOPIC METHODS

There are two general approaches for calculating the nuclear potential energy of deformation--selfconsistent microscopic methods and the macroscopic-microscopic method. In the microscopic methods, one usually starts with a given nucleon-nucleon potential and solves the many-body Schrödinger equation by means of the Hartree-Fock approximation. This can be done either with a realistic potential that is adjusted to reproduce fundamental data such as two-nucleon scattering data, or with an effective interaction that is adjusted to reproduce gross nuclear properties.

The realistic potentials of course lead to equations that are more difficult to solve. If the potential has a hard core, then the infinities associated with it must be removed by means of the approximations introduced by Brueckner. The resulting Brueckner-Hartree-Fock equations are so complicated that they have been solved so far only for spherical nuclei [8,9].

The equations are simpler for a soft-core potential, where the ordinary Hartree-Fock method can be applied. At deformations away from a local minimum the potential energy is calculated by applying an external field and solving the resulting constrained Hartree-Fock equations. In this way the potential energy has now been computed as a function of the quadrupole moment for some medium-weight nuclei such as  $^{108}\text{Ru}$  [10]. However, computational difficulties have prevented the extension of these calculations to heavy nuclei. For heavy spherical nuclei the calculated total binding energies are substantially smaller than the experimental values [11]. Although the agreement would be improved somewhat by including the second-order correction to the Hartree-Fock energy [12], this correction has not yet been calculated for deformed nuclei.

A major difficulty associated with the use of realistic potentials is the necessity to calculate the exchange terms in the Hartree-Fock equations. This difficulty can be eliminated by choosing an effective interaction for which the exchange terms are easy to calculate. Or alternatively, the exchange effects can be absorbed into the effective interaction [13,14]. With either approach the higher-order corrections to the first-order energy are absorbed into the interaction through a readjustment of its parameters.

Although several effective interactions have been proposed, the only one that is used in practice for the calculation of fission barriers is Skyrme's interaction [15] as simplified by Vautherin and Brink [16]. This interaction is easy to use because most of its terms contain delta functions and because saturation is achieved by means of a three-body term. The six adjustable parameters of the interaction are related loosely to the coefficients of the five dominant terms in the semiempirical nuclear mass formula

(corresponding to the volume, surface, Coulomb, volume-asymmetry, and surface-asymmetry energies) and to the spin-orbit interaction strength.

The Skyrme interaction has now been used by Flocard, Quentin, Kerman, and Vautherin to compute the potential energy as a function of the quadrupole moment for several isotopes of cerium [17] and more recently for  $^{240}\text{Pu}$  [18]; we will learn about such calculations later in this session from Quentin [19]. The calculated height of the second peak in the barrier for  $^{240}\text{Pu}$  is 19 MeV, which is substantially higher than the experimental value of 5.35 MeV [20]. This large discrepancy probably arises from a combination of three factors: (1) The results have not converged as a function of the basis size. (2) The parameters of the Skyrme interaction yield a surface energy that is too large compared to the Coulomb energy. (3) Mass-asymmetric deformations are not included. When these three points are taken care of we can expect such calculations to reproduce experimental fission barriers with satisfactory accuracy. This is the most promising of the microscopic approaches, and perhaps four years from now at the fourth IAEA fission symposium a substantial fraction of the fission barriers discussed will be computed selfconsistently in terms of such an effective interaction.

### 3. MACROSCOPIC-MICROSCOPIC METHOD

But at present nearly all fission barriers are calculated by means of the second approach--the macroscopic-microscopic method. This method synthesizes the best features of two complementary approaches: The smooth trends of the potential energy (with respect to particle numbers and deformation) are taken from a macroscopic model, and the local fluctuations are taken from a microscopic model. The method in its present form was developed in 1966 by Strutinsky [21] and has since revolutionized the calculation of fission barriers. The idea of a macroscopic-microscopic method had been introduced earlier by Swiatecki [22] and others.

In this method, which is suitable for treating nuclear systems that contain a large number of particles, the total nuclear potential energy of deformation is written as the sum of two terms,

$$V = V_{\text{macroscopic}} + \Delta V_{\text{microscopic}}$$

The first term is a smoothly varying macroscopic energy that reproduces the broad trends of the potential energy. In a heavy nucleus it accounts for about 99.5% of the 2000 MeV total binding energy and for about 95% of the 200 MeV variation in energy during fission. The second term contains oscillating microscopic corrections that arise because of the discreteness of the individual particles. The most important of these purely microscopic contributions are the shell and pairing corrections. For a tightly bound nucleus in its ground state the total microscopic correction is over 10 MeV in magnitude, but in other situations it is usually somewhat less.

The nuclear potential energy of deformation is calculated by means of the macroscopic-microscopic method in five steps: (1) The overall geometrical shape of the nucleus is first specified, and (2) the macroscopic part of the energy is calculated for this shape. (3) The single-particle potential felt by a neutron or proton is generated, and (4) the Schrödinger

equation is solved for the single-particle energies. (5) These energies are then used to calculate the microscopic (shell and pairing) corrections. The total potential energy is given finally by the sum of the macroscopic energy calculated in step 2 and the microscopic corrections calculated in step 5. These steps have received considerable study, and several methods have evolved for handling each of them.

### 3.1. Nuclear shapes

In fission, as well as in the related areas of heavy-ion reactions and nuclear ground-state masses and deformations, at least four collective coordinates are required to describe the most important shapes that arise. These are (1) a separation coordinate, which specifies the overall separation of the mass centers of the two nascent or separated fragments or colliding ions, (2) a mass-asymmetry coordinate, which specifies the amount of mass in one fragment relative to the other, (3) a fragment elongation coordinate, which specifies the overall elongation of the fragments, or alternatively the radius of the neck between them, and (4) an axial-asymmetry ( $\gamma$ ) coordinate, which specifies the flattening of the shape about its symmetry axis. Because of computational difficulties the latter coordinate is not included in most studies in fission. Our discussion is therefore sometimes restricted to axial symmetry, but the generalization to axially asymmetric shapes is straightforward.

The methods for describing such shapes fall into two major classes. The first class is an expansion about some basic shape, such as a sphere, a spheroid, or a Cassinian oval. For example, shapes close to a sphere are described conveniently by expanding the radius vector to the nuclear surface in a series of spherical harmonics. If the shape is elongated it is better to absorb some of the deformation into the basic shape and expand about a spheroid (ellipsoid of revolution). This can be done either by means of the coordinates  $\epsilon_1$  used by Nilsson and others [1, 2, 23-29], or by writing  $\rho^2$  as a polynomial in  $z$ , which is the method used by Lawrence, Hasse, Strutinsky, Pauli and others [3, 5, 30-35]. If the shape has already developed an appreciable neck it is sometimes advantageous to expand about a Cassinian oval, which can absorb some of the necking as well as elongation into the basic shape; this method is used by Cherdantsev and coworkers [36] and by Pashkevitch [37].

The second class of methods describes the shape in terms of two bodies rather than a single body. In these two-center parametrizations each end of the nucleus is usually represented by a portion of a spheroid. In the most simple version the two spheroids intersect in an undesirable cusp [38], but this cusp may be removed by connecting portions of the two end spheroids smoothly with a third function that describes the neck region. In the method used by Greiner, Mosel, and their coworkers [39-43], precisely one-half of each end spheroid is used in forming the shape, which unfortunately prevents the description of diamond-like nuclear ground-state deformations and some important shapes that arise in heavy-ion reactions. In another method [44-52], arbitrary portions of the two end spheroids are connected smoothly by a quadratic neck function.

Because an expansion method is usually better for describing nuclear ground-state deformations and the early stages of fission, whereas a two-center method is usually required for describing the later stages of fission and heavy-ion reactions, it is desirable to define the collective coordinates

in some parametrization-independent way that permits a connection to be made between the various methods. Of course the ideal choice would be to define the coordinates so that the resulting inertia matrix is everywhere diagonal and constant. This is in general impossible to accomplish, and the best that we can achieve at present is to define the coordinates in terms of physically measurable quantities.

For symmetric shapes a good choice involves the use of successive central moments of one-half of the shape distribution [53]. Then the separation coordinate is simply the distance between the centers of mass of the two nascent or separated fragments, and the fragment elongation coordinate is the root-mean-square extension of a fragment about its center of mass. As Sierk will discuss later in the symposium, this choice has already proved useful for displaying dynamical paths in fission and heavy-ion reactions [51]. The mass-asymmetry coordinate may be defined conveniently (and unambiguously) as the difference between the masses to either side of the point midway between the ends of the shape [3, 5, 33]. For shapes with a well-defined neck a more pleasant choice would involve the masses to either side of the neck, but in practice the two definitions are approximately equivalent because in such cases the volume in the neck region is small.

### 3.2. Macroscopic energy

Once the nuclear shape is specified, the macroscopic energy must be calculated for this shape. This usually is done by expanding the nuclear energy in powers of  $A^{-1/3}$  and  $[(N-Z)/A]^2$ . Truncating the expansion at the  $A^{2/3}[(N-Z)/A]^2$  term leads to the liquid-drop model, where the two shape-dependent terms are the cohesive surface energy and the disruptive Coulomb energy.

The inclusion of higher-order terms in the expansion leads to the droplet model, which takes into account effects that are associated with the finite size of nuclei, such as nuclear compressibility [54-56]. Myers and Swiatecki have now determined a preliminary set of constants for the droplet model [56] from adjustments to nuclear ground-state masses and fission-barrier heights and from statistical calculations. The resulting curvature-energy constant is zero. The effective surface-asymmetry constant, which regulates how rapidly fission barriers are lowered with the addition of neutrons, is significantly larger for heavy nuclei than the value in their earlier liquid-drop model [57]. As Howard will describe in the next paper [50], this makes it unlikely that superheavy nuclei can be formed by multiple neutron capture.

The condition that must be satisfied in order for the nuclear energy to be expanded in this way is that the surface diffuseness be small compared to the extension of the neighboring volume region. This condition breaks down for light nuclei and for shapes with small necks, for example near the scission point in fission and near the point of first contact in heavy-ion reactions. When calculating the energy of such shapes it is necessary to take into account the finite range of the nuclear force.

This could be done by treating an effective nucleon-nucleon interaction in some statistical approximation such as the Thomas-Fermi method [54, 58, 59]. However, in practice such calculations have been limited either to small deformations [60] or to two light spherical nuclei specified by a single separation coordinate [61, 62].

A simpler method has been developed recently for including finite-range effects. In this method the nuclear macroscopic energy is calculated in terms of a double volume integral over a Yukawa function. As Krappe will discuss later in this session [63], this leads to several important consequences, such as a reduction in the stiffness of light nuclei with respect to deformation. This lowers the fission barriers of nuclei near silver by about 10 MeV relative to those calculated with the liquid-drop model and shifts the critical Businaro-Gallone point (where stability against mass asymmetry is lost) to  $Z^2/A = 23$ , in approximate agreement with recent experimental evidence. The reduced stiffness also leads to a secondary minimum in the potential energy of  $^{40}\text{Ca}$  and certain other light nuclei, which provides a natural interpretation of the rotational states observed in these nuclei. In addition, experimental interaction-barrier heights for systems ranging from  $^{40}\text{Ca} + ^{16}\text{O}$  and  $^{208}\text{Pb} + ^4\text{He}$  to  $^{238}\text{U} + ^{84}\text{Kr}$  are reproduced to within 5% accuracy. This method also provides a way to calculate the nuclear macroscopic energy corresponding to the inner surface of a bubble nucleus [64].

### 3.3. Single-particle potential

Once the nuclear shape is specified and the macroscopic energy is calculated, the next step is to generate the single-particle potential for this shape. We know of course that the true potential is nonlocal and that it would require a selfconsistent calculation for its determination. But the great virtue of the macroscopic-microscopic method is that single-particle effects can be extracted approximately from a local static potential that is not generated selfconsistently.

Figure 2 illustrates our qualitative expectations concerning the spin-independent part of the nuclear potential. Because the single-particle potential arises from the interaction of a nucleon with its close neighbors, it is roughly constant in the nuclear interior and rises to zero within a surface region whose thickness is approximately independent of nuclear size and position on the surface. For separated nuclei the potential has similar features concentrated in each of the individual nuclei. This means that near the scission point in fission, or near the point of first touching in heavy-ion reactions, the potential is roughly constant in the interior of each nucleus and is elevated somewhat in the neck region. The overall geometrical shape of the potential follows closely that of the nucleus.

The potentials that have been developed for approximating this behavior fall into two general classes: modified oscillator potentials that rise to infinity at large distances, and diffuse-surface potentials that go to zero at large distances. Modified oscillator potentials are usually obtained by starting with a potential that rises parabolically to infinity from either one or two centers. An angular-momentum correction term proportional to  $\ell^2$  is then added, which in effect makes the potential rise more slowly near the center and faster near the nuclear surface. In an ordinary (one-center) potential, which has been studied extensively by Nilsson and others [1, 2, 21, 23-29, 32, 65, 66], the minimum of the original oscillator potential always occurs at the nuclear center. However, for sufficiently large deformations it is possible that the  $\ell^2$  correction term leads to a potential that in effect has two centers [67]. In the potential commonly referred to as a two-center potential, which has been used by Cherdantsev, Greiner, Mosel, and others [36, 39-43, 52], two separate minima occur in the original oscillator potential itself. At first sight this may seem clearly preferable. However,



when the fragment centers separate, the two-center potential rises several times as rapidly in the neck region as would be expected from fundamental considerations. This leads to the possibility that some of the conclusions based on this potential are associated with this spurious feature.

There are also two major types of diffuse-surface potentials. The first type is obtained by generalizing a spherical Woods-Saxon potential to deformed shapes. In the generalization used by Pashkevitch, Strutinsky, Pauli, and others [3, 5, 32-35, 37, 68], the potential's normal diffuseness is to first order constant over the surface. The resulting generalized Woods-Saxon potential is satisfactory for most shapes, but contains unphysical features when the neck radius is smaller than the diffuseness parameter. It therefore cannot be used to describe shapes near the scission point in fission or near the point of first touching in heavy-ion reactions.

The second type of diffuse-surface potential is generated by folding a Yukawa function over a uniform sharp-surface generating potential whose shape corresponds to the given nuclear shape [45-50]. In other words, a finite square-well potential of the appropriate depth and geometrical shape is converted into a diffuse-surface potential by folding a Yukawa function over it; the range of this function is chosen to reproduce the desired surface diffuseness. For small deformations the resulting potential is very close to a generalized Woods-Saxon potential. The major advantage of this folding procedure is that it can be used to generate easily a potential for any conceivable shape, including the transition for shapes with small necks to a potential concentrated in each of two individual nuclei, or vice versa. The potentials shown in Fig. 2 were generated in this way.

Besides the spin-independent part of the potential, there is an additional potential arising from the interaction between the nucleon spin and orbital angular momentum. Finally, protons feel a Coulomb potential, which is calculated easily by assuming that the nuclear charge is distributed uniformly within the nuclear surface or within the nuclear generating potential. However, in studies with oscillator potentials the Coulomb potential usually is not included explicitly, but its effects are absorbed by readjusting the parameters of the nuclear part of the potential.

Irrespective of how it is generated, the final potential usually contains about six parameters that effectively describe the depth, radius, diffuseness, and spin-orbit strength of the potentials for neutrons and protons. In studies with oscillator potentials these parameters are usually determined from adjustments to experimental single-particle levels in heavy deformed nuclei. For diffuse-surface potentials some of the parameters can be obtained from statistical calculations [69]; the remainder are usually determined from adjustments to experimental single-particle levels in either heavy spherical or heavy deformed nuclei.

### 3.4. Solution of Schrödinger equation

Once the potential appropriate to a given shape is generated, the next step is to solve the Schrödinger equation for the single-particle energies. There are two general methods for doing this: expansion in basis functions and finite-difference methods. The expansion methods are usually several times as fast as the finite-difference methods for calculating single-particle energies with comparable accuracy [46, 47]. For most applications in fission

the preferred choice is to expand the wave function in a set of deformed harmonic-oscillator basis functions.

### 3.5. Microscopic corrections

Once the single-particle energy levels are solved for, the microscopic corrections to the potential energy must be extracted from them. The two most important of these corrections are the shell correction and the pairing correction,

$$\Delta V_{\text{microscopic}} = \Delta V_{\text{shell}} + \Delta V_{\text{pairing}} \quad .$$

They arise because of fluctuations in the actual distribution of levels relative to a smooth distribution.

These fluctuations are especially dramatic for a pure harmonic-oscillator potential, as shown in Fig. 3. For a shape of high symmetry, such as a sphere or a spheroid whose major axis to minor axis is in the ratio of two small integers, the levels group into highly degenerate shells [70]. For such a shape, the energy of the system is relatively lower for particle numbers that complete a shell than for intermediate particle numbers. At other deformations, the levels are distributed more uniformly. In an actual nucleus similar fluctuations in the single-particle levels give rise to microscopic corrections that oscillate with deformation and particle numbers. These are the oscillations that are responsible for deformed ground states, second minima in fission barriers, and asymmetric saddle-point shapes.

The primary theoretical justification for extracting the shell correction from single-particle energies is provided by the stationary property of the Hartree-Fock solution: To first order in the deviation of the actual nuclear density from a smooth density, the total Hartree-Fock energy is equal to the sum of single-particle energies

$$\sum_{n=1}^N \epsilon_n$$

calculated from a smooth single-particle potential, plus a smoothly varying term [3, 5, 9, 10, 65, 71, 72]. Therefore, to first order in nuclear density deviations, the fluctuations that we want to isolate are contained in this sum of single-particle energies. As Brack will discuss later in this session [71], second-order effects in the shell correction [72] are expected in general to be about 1 MeV in magnitude, but could be somewhat larger for spherical nuclei. These second-order effects are probably responsible for some of the remaining discrepancies between calculated and experimental results.

The extraction of the shell correction from the single-particle energies has a simple geometric interpretation, as illustrated in Fig. 4. First plot the energies  $\epsilon_n$  at a given deformation vs the single-particle number  $n$ . For a macroscopic system without single-particle effects all the energies would lie on a smooth curve, but the discreteness of the single particles causes some fluctuations about a monotonically increasing function of  $n$ . The discrete energies  $\epsilon_n$  can be regarded as a staircase function formed by horizontal and vertical lines through the points. Next remove the local

fluctuations of the staircase function while retaining its long-range behavior by passing a smooth curve  $\bar{\epsilon}(n)$  through it. Then the shell correction for a specified number of particles  $N$  is given simply by the difference between the areas under the staircase curve and the smooth curve up to  $N$ ; that is,

$$\Delta V_{\text{shell}} = \sum_{n=1}^N \epsilon_n - \int_0^N \bar{\epsilon}(n) \, dn \quad .$$

A variety of methods have been proposed for determining the smooth curve  $\bar{\epsilon}(n)$ . Unfortunately, most of these methods work only for certain simple potentials and cannot be used, for example, with potentials that contain a spin-orbit term. For realistic potentials of arbitrary shape, the most satisfactory way at present to determine  $\bar{\epsilon}(n)$  is by use of Strutinsky's method [21], which was described to us at the second IAEA fission symposium by Strutinsky himself [32]. We need not repeat the technical details of his method here.

An alternative method has been studied for calculating the shell correction from the high-temperature dependence of the entropy of the single-particle system on excitation energy [73-77]. For heavy nuclei the results obtained by use of this method agree with those obtained by use of Strutinsky's method to within about 0.5 MeV. Perhaps this method will be discussed during the session on thermodynamic properties of nuclei.

The second type of single-particle correction--the pairing correction--arises from the short-range interaction of correlated pairs of nucleons moving in time-reversed orbits. This is the most important and easily treated of the many residual interactions felt by a nucleon. Relative to the energy without pairing, this interaction always lowers the energy. But relative to the pairing energy of a smooth distribution of levels representing an average nucleus, the pairing correction can have either sign. The lowering in energy is larger when more pairs of nucleons are able to interact, which occurs when the level density near the Fermi surface is high. This is opposite to the behavior of the shell correction, and this leads to a partial cancellation of the two corrections. Because the shell correction is larger, it determines the main trends of the total single-particle correction.

The essential features of the pairing correction can be described in terms of a constant pairing interaction between a given number of pairs of particles. Then a standard pairing calculation in the BCS approximation gives the lowering in energy for the actual levels. A similar calculation for the same number of particles distributed smoothly according to  $\bar{\epsilon}(n)$ , or in practice distributed uniformly, gives the lowering for an average nucleus. The difference between the lowering for the actual levels and the lowering for the smooth levels is the pairing correction.

Once the fluctuating shell and pairing corrections are calculated, the final step is to add them to the smooth macroscopic energy calculated in step 2 to obtain the total potential energy.

These methods have now been used by several groups to calculate the fission barriers for dozens of nuclei [1-5, 24-28, 32-37, 41-43, 47-50, 52, 65, 66, 68]. In most instances the results obtained by the different groups are

qualitatively similar, although some differences exist. Rather than trying to review all of this work, we would like to describe instead some new results that we have obtained recently at Los Alamos.

#### 4. NEW CALCULATIONS

We have performed two separate new calculations: one with the folded Yukawa potential and the other with the modified oscillator potential. Both of these calculations are limited to even nuclei. In the former calculation, there are three main differences compared to previous studies with this potential. First, we now use the droplet model in place of the liquid-drop model for calculating the macroscopic energy. The constants of the droplet model are a preliminary set determined by Myers and Swiatecki in January 1973 [56]. We may therefore regard the present results as one step in the complex iteration that is required for a final determination of these constants.

Second, we now investigate a larger part of the deformation space when determining the extrema of the potential-energy surfaces. Our exact procedure is described in the appendix, but the idea is that in the region that includes the first and second saddle points and the second minimum we minimize the potential energy calculated in the three-quadratic-surface parametrization with respect to a necking coordinate. During this minimization the eccentricities of the two ends of the nucleus and the distance between the centers of mass of the two nascent fragments are held fixed at the values corresponding to the  $y$  family of shapes [45, 47]. In the region of the ground state a somewhat different constraint on the three-quadratic-surface parametrization is used. The ground-state energy is also calculated by use of the two coordinates  $c$  and  $c_0$  in Nilsson's perturbed-spheroid parametrization [1, 2, 23-29], which for most deformed nuclei yields a lower energy. In the region somewhat beyond the second saddle point down to scission the potential energy is no longer minimized (because the nucleus is on the side of a steep hill), but is calculated instead for shapes along the most probable idealized liquid-drop-model dynamical path for fissility parameter  $x = 0.8$  [44, 51] and for asymmetric perturbations about these shapes. The fissility parameter is defined as the ratio of the Coulomb energy of a spherical sharp-surface drop to twice the spherical surface energy.

In all regions the final potential energy is displayed in terms of a fission coordinate  $r$  defined as the distance between the mass centers of the two halves of the dividing nucleus and a mass-asymmetry coordinate  $(M_1 - M_2)/M_0$  defined as the difference between the masses to either side of the point midway between the ends of the shape. For computational convenience the fission coordinate for an asymmetric shape is chosen equal to the fission coordinate for the corresponding symmetric shape.

The third difference is that we are now using a new set of parameters for the single-particle potential. Our original set of parameters was determined from statistical calculations and from adjustments to experimental single-particle levels in the heavy spherical nucleus  $^{200}\text{Pb}$  [47]. In the new set, which has been determined in collaboration with Nilsson, we have re-determined the range of the Yukawa folding function (which regulates the surface diffuseness of the potential) and the spin-orbit interaction strengths for neutrons and protons from adjustments to experimental single-particle levels in heavy deformed nuclei. The resulting values of these constants are

$$a = 0.8 \text{ fm} \quad ,$$

$$\lambda_n = 36 \quad ,$$

and

$$\lambda_p = 34 \quad ;$$

the well depths for neutrons and protons and the radius of the spherical generating potential remain unchanged [47]. The potential's surface is now 11% thinner than previously, and the spin-orbit interactions for neutrons and protons are now stronger by 12% and 6%, respectively. These differences arise mainly from requiring the calculated single-particle levels to reproduce the observed gap at  $N = 152$  in the experimental neutron levels. With these new parameters, the experimental levels in  $^{208}\text{Pb}$  are reproduced slightly less accurately than before. It appears extremely difficult to find a single set of parameters that reproduces satisfactorily the experimental levels in both spherical and deformed nuclei.

In the new calculation with the modified oscillator potential, the only difference compared to a previous study with this potential [28] is the replacement of the liquid-drop model by the droplet model; we therefore omit the intermediate results calculated with this potential and present only the final comparison with experimental data.

We show in Fig. 5 the barriers that are calculated with the folded Yukawa potential for a group of actinide nuclei. The dashed curves give the potential energy for symmetric deformations and illustrate what we believed about fission barriers four years ago in Vienna. At that time we thought that a second minimum existed between two peaks in the barrier and that it was responsible for shape isomers and intermediate structure in fission cross sections.

This second minimum occurs because of special degeneracies in the single-particle energies for shapes of high symmetry. In particular, when the nucleus is approximately twice as long as it is wide, the energy is lowered substantially for particle numbers that correspond to actinide nuclei. Because of this--and because the macroscopic contribution to the energy is close to its saddle point and hence relatively flat at this deformation--the resulting fission barriers of most actinide nuclei contain a second minimum.

But in Vienna we still could not understand why the calculated barrier heights reproduced the experimental values so poorly, or why actinide nuclei usually divide asymmetrically. Shortly thereafter several calculations [2-5, 26-28, 33-37, 42, 47, 49] indicated that the second saddle point in the fission barriers of the lighter actinide nuclei is lowered by several MeV when mass-asymmetric deformations are introduced, as indicated here by the solid curves. For the heavier actinide nuclei the energy of the second saddle point is reduced much less by mass-asymmetric deformations.

The first peak is found to be stable with respect to mass asymmetry. However, studies by Larsson, Pashkevich, Pauli, and others [1, 66, 68] have demonstrated that for the heavier actinide nuclei the first peak is unstable with respect to axial asymmetry (gamma deformations); this lowers the energy by over 2 MeV in some cases.

The variation of the calculated heights of the equilibrium points with neutron number arises primarily from single-particle effects. However, the variation of the heights with proton number is associated also with large changes in the macroscopic energy. Increasing the proton number  $Z$  pulls in the maximum of the macroscopic energy to make the first peak higher than the second. Conversely, decreasing  $Z$  pushes out the macroscopic maximum to make the second peak higher than the first.

We come finally to a new observation that is apparent in Fig. 5: For small neutron numbers (below about 146 in these calculations), the asymmetric second saddle point is actually split into two individual saddle points separated by a third minimum! Such a splitting is possibly responsible for the broad resonance observed in the fission cross sections of the compound nuclei  $^{231}\text{Th}$ ,  $^{232}\text{Th}$ , and  $^{234}\text{Th}$  [78, 79]. These data have always been interpreted as implying that the first saddle point and second minimum in the barrier are substantially higher than the calculated values. But it now appears likely that these experimental values refer instead to the middle saddle point and third minimum in the barrier, which offers a simple resolution of the thorium anomaly. These third minima are associated with a shift in the location of the asymmetric second saddle point from a large distortion  $r$  to a smaller distortion as the neutron number increases. Similar third minima are also present in some previous calculations for thorium isotopes with both the generalized Woods-Saxon potential [37] and the modified oscillator potential [28], but the possible significance of these minima was not realized until now. It is conceivable that such third minima are a spurious feature of limited shape parametrizations, but this can be checked through further work. The possibility of this additional complexity in the vicinity of the asymmetric second saddle point means that great care should be taken when determining barrier heights from fission cross sections [6], when calculating spontaneous-fission half-lives [35, 80, 81], and when correlating the properties of fission isomers [7].

Some of these points are appreciated better in a contour map where the mass-asymmetry coordinate is included explicitly. Two such maps are shown in Fig. 6: one for  $^{236}\text{U}$ , where the experimental most probable mass division is asymmetric at low excitation energy, and the other for  $^{250}\text{Fm}$ , where the most probable mass division is symmetric. We may think of the ground states of these nuclei as lakes that are separated from the regions to the right by mountain ranges. Each range contains one or more peaks, additional lakes, and passes (saddle points), although in other respects they are different in character. For example, the  $^{250}\text{Fm}$  range is significantly narrower than the  $^{236}\text{U}$  range; this arises because of the larger Coulomb force in  $^{250}\text{Fm}$ .

For each nucleus the first lake, first pass, and second lake occur for symmetric shapes. (Axially asymmetric distortions, which are not considered here, would lower the first pass by about 0.3 MeV for  $^{236}\text{U}$  and by about 2 MeV for  $^{250}\text{Fm}$  [1].) Because of its high elevation the symmetric peak for  $^{236}\text{U}$  is snow-capped. However, it is not necessary to go over this forbidding peak in order to fission: the asymmetric route around this mountain is 3.7 MeV lower. In addition, the asymmetric lake that separates the two asymmetric passes provides a convenient resting place. Beyond this lake, the asymmetric route for  $^{236}\text{U}$  divides. One branch leads over an asymmetric pass down into another small lake in the symmetric valley. The second branch leads over a slightly higher and more asymmetric pass into an asymmetric valley. These two valleys are separated by an asymmetric snow-capped peak. We have not yet investigated

these valleys in detail, but if a similar topology occurs for nuclei near radium it could possibly be responsible for the experimentally observed three-peaked mass distributions for these nuclei. In contrast, the symmetric peak for  $^{250}\text{Fm}$  is relatively low in elevation, and only 1.2 MeV is gained by taking the asymmetric route around this mountain.

Apart from the equilibrium points, such potential-energy surfaces are not invariant under a change of coordinates. It is well known that valleys can be transformed into ridges, and vice versa, by coordinate transformations [82]. We therefore do not attach a great deal of significance to the apparent valleys or ridges on the steep hillside between the saddle and scission regions. The answer to the motion in this region must await a proper dynamical calculation; some aspects of dynamics will be discussed later in the symposium by Pauli, Sierk, and others [35, 51].

We do note, however, that beyond the last saddle point the apparent stability shifts between symmetric and asymmetric shapes. Such shifts arise from oscillations in the single-particle corrections. From fundamental considerations one expects these oscillations to continue well past the saddle-point region provided that the nucleus continues to elongate as it does along the path chosen here.

However, the opposite result was obtained recently by Mustafa, Mosel, and Schmitt in some calculations with the modified two-center oscillator potential [41-43]. Figure 7 shows their calculated potential-energy surface for  $^{236}\text{U}$ , which is obtained by minimizing the potential energy with respect to overall elongation and with respect to the difference in the transverse semiaxes of the nascent fragments. Note the apparent valley that extends from the scission region all the way back to the second saddle point.

Part of the difference between these two results for  $^{236}\text{U}$  stems from the use of different single-particle potentials, as illustrated in Fig. 8. Whereas the folded Yukawa potential is practically constant along the symmetry axis, the two-center oscillator potential is 5 MeV higher in the middle than in the center of either nascent fragment, even though this particular two-center saddle-point shape does not contain an indented neck! This early rise of the two-center potential in the neck region contributes somewhat to an early formation of shell structure associated with the fragments.

But the main difference arises because different shapes are considered. In our calculations the distance between the fragment mass centers increases continuously, whereas Mustafa, Mosel, and Schmitt minimize the potential energy with respect to this coordinate. This makes it possible for the nucleus to adjust its length as its neck radius is decreased in order to remain in a local asymmetric valley. Similar local valleys are evident in the potential-energy surfaces calculated by Pauli with a generalized Woods-Saxon potential and the liquid-drop model [5]. These valleys are aligned approximately along fixed values of the distance between mass centers  $r$ . With increasing  $r$  the nucleus passes from one valley into another, which is the situation in Fig. 6. When the nucleus adjusts its length to remain in an asymmetric valley, it arrives at the scission region with a more compact shape; this partially explains why the scission energy is higher in Fig. 7 than in Fig. 6.

## 5. ENERGIES OF THE LOCAL MINIMA AND SADDLE POINTS

We turn now to a comparison between calculated and experimental energies of the equilibrium points in the potential-energy surfaces.

### 5.1. Folded Yukawa potential

Figure 9 compares the calculated and experimental ground-state masses of heavy even nuclei; both spherical nuclei near  $^{200}\text{Pb}$  and deformed actinide nuclei are included. The calculations reproduce the general trends of the experimental results, but some systematic discrepancies remain, as shown in the lower portion of the figure. Similar discrepancies have been observed previously [2-5, 24, 28, 29, 57]. When viewed over a broad region of nuclei, the discrepancy in the ground-state masses oscillates with particle number. The maximum error occurs for  $^{222}\text{Th}$ , where it is 2.6 MeV in magnitude. For the isotopes of a given actinide element, the minimum in the calculated ground-state single-particle correction is always at neutron number  $N = 152$ . This is because the parameters of the single-particle potential are adjusted to reproduce the gap at  $N = 152$  in the experimental single-particle levels of ground-state nuclei. However, this minimum in the ground-state single-particle correction is observed experimentally only for the heavier actinide nuclei ( $Z \geq 100$ ). For the isotopes of a given actinide element, the difference between the experimental and calculated masses is an increasing function of neutron number.

Provided that it does not affect the potential energy at larger deformations in the same way, such an error in the calculated ground-state mass can propagate into the calculated heights of the saddle points and remaining minima in the potential-energy surface. This is illustrated in Fig. 10 for even actinide nuclei between thorium and fermium. The solid curves give the appropriate theoretical height relative to the calculated ground-state energy, and the dashed curves give the corresponding height relative to the experimental ground-state energy. The difference between the solid and dashed curves is therefore simply the error in the calculated ground-state energy. On the other hand, an error in a term that is independent of deformation, such as the volume energy [28], would not affect the calculated heights of the remaining extrema.

The first column of Fig. 10 compares the theoretical and experimental heights for the first saddle point. The theoretical results do not include the effects of axially asymmetric deformations, which would lower somewhat the calculated heights for the heavier nuclei [1]. When allowance is made for this lowering, the theoretical heights (relative to either the calculated or experimental ground-state energies) are slightly lower than the experimental heights. The second column is a similar comparison for the height of the second minimum. Apart from the results for thorium, the theoretical and experimental values are in approximate agreement, although both the solid and dashed theoretical curves show a stronger dependence on neutron number than is observed experimentally.

For isotopes of thorium the calculated second minima are about 3 MeV lower than the experimental values commonly attributed to this minimum. This large discrepancy--together with a similar discrepancy at the first saddle point--constitutes the thorium anomaly [34, 78, 79]. We suggest that a



possible resolution of this anomaly is the third asymmetric minimum in the barrier, whose calculated heights agree with the experimental values to within 0.5 MeV. The discrepancies for thorium that are evident in the first column are reduced somewhat when the experimental heights that are commonly attributed to the first saddle point are compared instead with the calculated heights for the lower of the two asymmetric saddle points that surround the asymmetric third minimum. But these calculated heights are still lower than the experimental ones by about 2 MeV.

For plutonium the experimental heights of the second minimum are systematically lower by about 0.2 MeV for odd-neutron isotopes than for even isotopes. As pointed out by Nilsson [67], this implies that the pairing gap is smaller by this amount at the second minimum than at the ground state. This arises because the single-particle levels have a larger shell at the second minimum--where the shape has a ratio of axes of approximately 2/1--than at the ground state. Such odd-particle fluctuations in the height of the second minimum are evident in the calculations of Ref. [20].

The third column of Fig. 10 compares the theoretical and experimental heights of the second saddle point. For thorium and uranium both the solid and dashed theoretical curves are somewhat lower than the experimental values and show a more rapid variation with neutron number. For plutonium and curium the dashed curves are in approximate agreement with the experimental values, but the solid curves vary too rapidly with neutron number.

In some calculations of fission-barrier heights [34, 80, 86], the values of two constants in the liquid-drop model are adjusted in order to reproduce optimally the experimental heights of the second saddle point. Because the calculated heights are affected to an unknown extent by the poorly understood systematic error in the calculated ground-state energies, great care must be exercised when attempting to determine liquid-drop-model constants in this way. As an extreme example, had experimental rather than calculated ground-state energies been used in the previous studies [34, 80, 86], the resulting values of the surface-asymmetry constant  $K$  would have been substantially lower.

At present we are calculating the fission barriers for a broad region of lighter nuclei. The calculated barrier height for  $^{210}\text{Po}$  is 23.3 MeV relative to the calculated ground-state energy, and is 22.0 MeV relative to the experimental ground-state energy. These theoretical heights are to be compared with 21.4 and 20.5 MeV obtained in two different experiments [87], and with the value of 24.7 MeV calculated by Mosel with the modified two-center oscillator potential and the liquid-drop model [41].

## 5.2. Modified oscillator potential

In the next three figures we present some analogous results obtained with the modified oscillator potential. In Fig. 11 we see the effect of axially asymmetric (gamma) distortions at the first saddle point; this will be discussed in greater detail later in this session by Larsson [1]. We note the excellent agreement with experimental results that is achieved for the heavier nuclei by including axially asymmetric distortions. However, there are some significant deviations between the calculated and experimental results for the lighter isotopes of thorium and uranium.

The results shown in Figs. 12 and 13 for the second minimum and the second saddle point, respectively, are calculated in the same way as those of

Ref. [28] with two exceptions: We now use the droplet model for the macroscopic energy and include a zero-point energy of 0.5 MeV at the ground state and second minimum. The strength of the pairing interaction is taken to be independent of deformation. In Fig. 12 we see that although the experimental and calculated heights of the second minimum are in approximate agreement, the calculated values depend more strongly on neutron number than do the experimental values. In particular, the calculated values contain a minimum at  $N = 144$  and a maximum at  $N = 152$ , whereas the experimental values are approximately independent of neutron number (apart from the odd-particle fluctuations discussed earlier).

As seen in Fig. 13, the calculated heights of the second saddle point for uranium and plutonium are fairly constant as functions of neutron number and are in excellent agreement with the experimental results. The agreement is also very good for curium, whereas for thorium the calculated values are about 1 MeV higher than the experimental values and vary somewhat too rapidly with neutron number.

For the heavier actinide nuclei there are no experimental measurements on the height of the second saddle point. However, the spontaneous-fission half-life for  $^{258}\text{Fm}$  is unexpectedly short compared to that of the neighboring nucleus  $^{256}\text{Fm}$ . In particular, the half-life of 380  $\mu\text{s}$  for  $^{258}\text{Fm}$  is only  $4 \times 10^{-8}$  times that for  $^{256}\text{Fm}$  [88, 89]. This may indicate that for  $^{258}\text{Fm}$  the second saddle point is lower than the ground state [80]. This could also be true for  $^{244}\text{Fm}$ , which has a short spontaneous-fission half-life of 3.3 ms [90]. This indirect evidence therefore suggests that the heights of the second saddle points for  $^{244}\text{Fm}$  and  $^{258}\text{Fm}$  are about zero. This is reproduced approximately by the calculations shown in Fig. 13.

### 5.3. Comparison of folded Yukawa and modified oscillator potentials

For both the folded Yukawa potential and the modified oscillator potential, the present calculations agree better with experimental results than previous calculations with these potentials [20, 28, 47, 49]. Of particular importance, the rapid variation of the height of the second saddle point with neutron number that was predicted by the old calculations but is not observed experimentally is reduced substantially. For the modified oscillator potential this improved agreement stems from the use of the droplet model for the macroscopic energy. For the folded Yukawa potential the introduction of additional shape coordinates and the use of different parameters for the single-particle potential also contribute. Unfortunately we are not able to answer the delicate question of whether the improved agreement arises because of the higher-order terms in the droplet model or simply because of a better set of constants for the leading terms.

In carrying out this study we have come to appreciate the remarkable similarity in the results calculated for actinide nuclei by use of potentials that at first sight seem radically different. Similarities near the ground state are understood easily because we adjust the parameters of each potential to reproduce the same experimental single-particle levels in heavy deformed nuclei. But in addition the two calculations yield similar results at the second saddle point for detailed questions: For example, for which isotope does the maximum decrease in energy due to asymmetric distortions occur? And, for which isotope does the location of the asymmetric second saddle point shift from a large distortion  $r$  to a smaller distortion? The two

calculations answer both these questions in the same way to within an accuracy of  $\pm 2$  neutrons for all even nuclei between thorium and fermium. This suggests that the dependence of single-particle effects on deformation arises primarily from the overall geometrical shape of the potential rather than from fine details associated with it. This agrees with the conclusions obtained by Balian and Bloch on the basis of closed stationary paths in potentials [91].

But of course there are some differences in the results calculated with the two potentials. For example, compare the rapid increase in the height of the second saddle point with increasing neutron number just below 152 in the folded Yukawa calculations with the relatively constant behavior in the modified oscillator calculations. This difference comes about from effects both at the ground state and at the second saddle point. As an example, for plutonium the ground-state energy calculated with the folded Yukawa potential decreases by 1.1 MeV between  $N = 144$  and  $N = 152$  and the saddle-point energy increases by 1.0 MeV, which increases the height of the second saddle point by 2.1 MeV. In the modified oscillator calculations the corresponding values are 0.19 MeV and 0.02 MeV, which increases the height by only 0.21 MeV. At the ground state the differences arise because the single-particle level density near neutron number  $N = 144$  is slightly higher for the folded Yukawa potential than for the modified oscillator potential (even though both potentials are meant to reproduce the same experimental levels).

We find that the levels at the second saddle point are much less sensitive to changes in the parameters of the single-particle potential than are those near the ground state. The major differences at the second saddle point seem to arise because in the folded Yukawa calculations we vary the necking coordinate  $\alpha_2$  independently of the separation and asymmetry coordinates, whereas in the modified oscillator calculations the necking coordinate  $\epsilon_4$  has a prescribed dependence on the other coordinates.

Another difference is that the heights of the second saddle point do not decrease as rapidly with increasing proton number in the folded Yukawa calculations as in the modified oscillator calculations. This arises primarily because the second saddle point for heavy nuclei near  $^{252}\text{Fm}$ , for example, occurs near the macroscopic saddle point with the folded Yukawa potential, whereas with the modified oscillator potential it occurs at a somewhat larger deformation, where the macroscopic contribution is about 2 MeV lower. The main reason that the second saddle occurs at a smaller deformation with the folded Yukawa potential is that the single particle levels cross earlier.

In order to permit a better choice between the available single-particle potentials, and in order to determine the constants of these potentials more precisely, we need more direct experimental information at large deformations. This includes the determination of the nuclear shape and the identification of the single-particle states at the second minimum, for which some notable first steps have been taken [92-94].

We again stress that, despite these minor differences, the two potentials yield remarkably similar results for the fission barriers of actinide nuclei. It is therefore disconcerting to note the relatively large differences in the predictions for superheavy nuclei based on the two potentials [24, 25, 47-49]. In particular, the modified oscillator potential predicts that the eastern side of the island of superheavy nuclei (i.e., the side with neutron number greater than 184) is more stable than the western side, whereas

the folded Yukawa potential (as well as the Woods-Saxon potential) predicts that the western side is more stable.

We had originally thought that part of this difference was caused by having used experimental single-particle levels in  $^{208}\text{Pb}$  to determine the parameters of the folded Yukawa potential and single-particle levels in heavy deformed nuclei to determine the parameters of the modified oscillator potential. But now that we use levels in heavy deformed nuclei for both potentials the differences are even greater [50]! This comes about because the surface-diffuseness parameter for the folded Yukawa potential is now smaller, which makes this potential more like a square-well potential. We conclude that although satisfactory agreement with experimental results may be achieved for a limited region of nuclei through the adjustment of parameters in the single-particle potential, great care must be exercised when extrapolating the potential to new regions of nuclei.

## 6. FISSION-FRAGMENT MASS DISTRIBUTIONS

We come finally to the puzzle that has intrigued physicists ever since the discovery of fission: the preference of most actinide nuclei at low excitation energy to divide asymmetrically. We now understand this preference--as well as the preference in other situations for nuclei to divide symmetrically--in terms of single-particle effects superimposed on a smooth macroscopic background.

### 6.1. Origin of asymmetric instabilities

Let us examine these two contributions individually. As illustrated in Fig. 14, the saddle-point shapes for the macroscopic portion of the energy are stable against mass-asymmetric deformations for nuclei heavier than about silver and are unstable for lighter nuclei. Because the quantity plotted is equal to the stiffness against mass asymmetry divided by the corresponding inertia, the effective macroscopic stiffness against mass asymmetry increases sharply for heavier nuclei. In order for an asymmetric mass division to occur, a possible single-particle preference for asymmetry must be sufficiently strong to overcome this macroscopic preference for stability. Because the magnitude of single-particle effects remains approximately constant with increasing mass number, this increase in the stiffness of the macroscopic contribution suggests that sufficiently heavy nuclei will always prefer to divide symmetrically. Some recent calculations with the modified two-center oscillator potential support this observation [43].

We have already seen that the addition of single-particle effects to the macroscopic energy can lead to a high and sharp peak in the total potential energy as a function of the symmetric fission coordinate. This peak is caused by an unusually high single-particle level density near the Fermi surface for this particular shape. Any type of deformation that reduces this high level density leads to a decrease in the single-particle correction. Whereas the single-particle levels depend linearly upon symmetric deformations, they are to first order independent of asymmetric deformations. For large asymmetric deformations many levels remain practically constant, whereas some specific levels vary strongly [27]. When these specific levels are near the Fermi surface, asymmetric deformations can reduce the single-particle correction. Then, provided that the macroscopic energy does not increase too rapidly, the total potential energy should have an asymmetric path of lower energy leading around the symmetric peak [27, 96].

Two near-lying levels are affected strongly by an asymmetric perturbation when the matrix element of the perturbation between them is large. The matrix element of a mass-asymmetric perturbation is large between two states of opposite parity that have similar transverse and azimuthal wave functions and that have 0 and 1 node, respectively, in their wave functions along the symmetry axis  $z$ . This is illustrated in Fig. 15, where the neutron levels near the second saddle point of an actinide nucleus are shown as functions of mass asymmetry. These results are calculated with the modified oscillator potential. In terms of the asymptotic quantum numbers  $[Nn_z\Lambda\Omega]$ , the levels that are affected most by mass asymmetry are  $[40\Lambda\Omega]$  and  $[51\Lambda\Omega]$ . Four orbitals of each type occur between neutron number 130 and 170 at the second saddle point; it is the presence of these eight mass-asymmetry-favoring orbitals near the Fermi surface that leads to mass-asymmetric second saddle points in actinide nuclei. These same orbitals are also responsible for mass asymmetric saddle points in calculations with the folded Yukawa potential and with the generalized Woods-Saxon potential [5].

As the nucleus continues to deform past the saddle point, the development of the neck and ultimately the rise of the potential in the neck cause all levels to group into nearly degenerate pairs of levels of opposite parity. This occurs because the squeezing at the neck raises the energy of a state without a node at  $z = 0$  more than it raises the energy of a state with a node. As stressed by Andersen [97], these pairs of levels finally become the levels in the two individual fragments after scission. In this limit every level is affected by a change in mass asymmetry. However, because of the difficulty of mass transfer near scission, the mass split must be decided somewhat before this point. But in this way we see the connection between the effects of shell structure in the fragments and at the saddle point.

At the first symmetric saddle point of actinide nuclei the single-particle level density near the Fermi surface is also high, but such shapes are stable against mass asymmetry because the mass-asymmetry-favoring orbitals are not as close to each other there. On the other hand, axial-asymmetry-favoring orbitals are present near the Fermi surface at the first saddle point of the heavier actinide nuclei, which leads to axially asymmetric first saddle points in these nuclei.

## 6.2. Saddle-point properties

Although a few mysteries still remain, the main features of experimental fission-fragment mass distributions are now understood in terms of the calculated properties of the saddle points. At low excitation energy, most heavy nuclei ( $Z \geq 90$ ) divide primarily into one large fragment and one small fragment. For these nuclei, the second saddle point is calculated to be reflection-asymmetric in shape. Figure 16 shows for actinide nuclei the correlation that exists between the experimental most probable mass asymmetries and the values calculated at the second saddle point with the folded Yukawa potential.

If the mass distribution is determined at the second saddle point, then the experimental peak-to-valley ratio should be related exponentially to the difference between the energies of the second symmetric saddle point and the second asymmetric saddle point [101]. Such a correlation is presented in Fig. 17 for actinide nuclei; the folded Yukawa potential is used to calculate the differences in the energies of the saddle points.

What happens to the nucleus after it passes over the asymmetric second saddle point? It has two main choices: It can adjust its overall length in order to remain in an asymmetric valley of low potential energy created by the single-particle effects [5, 42, 43]. Or alternatively, it can increase its overall length in accordance with the preference of the macroscopic part of the energy. If this occurs, it moves out of the asymmetric valley of low potential energy onto another part of the multidimensional deformation space [5]. These two possible alternatives are illustrated by the potential-energy maps in Figs. 7 and 6, respectively. Perhaps some information on which alternative a nucleus chooses could be obtained from a careful examination of experimental fission-fragment kinetic energies. But it is more likely that we will have to wait for a proper dynamical calculation to provide the answer to this important question.

Experimental fission-fragment mass distributions for nuclei in the vicinity of radium ( $84 < Z < 90$ ) have three peaks; one corresponds to division into equal fragments and the others correspond to division into unequal fragments. Still lighter nuclei ( $Z \leq 84$ ) divide primarily into two equal fragments at all excitation energies for which the mass distributions are known. More recent experiments show that the mass asymmetry also decreases strongly for very heavy nuclei [102, 103]. In particular, the most probable mass split in the thermal-neutron-induced fission of  $^{257}\text{Fm}$  ( $\beta = 100$ ) is symmetric [103].

In our new calculations with the folded Yukawa potential, the saddle point for  $^{226}\text{Ra}$  is slightly asymmetric [ $(M_1 - M_2)/M_0 = 0.075$ ] and is 2.3 MeV lower in energy than the corresponding symmetric saddle point; this agrees qualitatively with most of the other calculations for radium isotopes [5, 28, 33, 47, 49]. We have not yet investigated the potential-energy surface for  $^{226}\text{Ra}$  for large distortions beyond the saddle point or for large mass asymmetry, but it is possible that an asymmetric valley similar to the one shown in Fig. 6 for  $^{236}\text{U}$  will appear. If so, the presence of such an additional valley may be responsible for the three-peaked mass distributions observed experimentally for nuclei near radium. On the other hand, odd-particle effects may be partially responsible, because the experimental mass distributions are for compound nuclei such as  $^{227}\text{Ac}$  and  $^{228}\text{Ac}$ , which contain one or more odd particles [104, 105].

For  $^{210}\text{Po}$  we find in our new calculations with the folded Yukawa potential that the potential energy is extremely flat near the saddle point. Although the small differences in potential energy in this region are comparable to the numerical accuracy of the calculations, the results taken at face value yield an asymmetric saddle point [at  $(M_1 - M_2)/M_0 = 0.092$ ] that is 0.25 MeV lower than the symmetric saddle point. The peak that separates them is only 0.25 MeV higher than the symmetric saddle point. Although the total potential energy is flat near the saddle point, the single-particle levels themselves vary strongly with deformation. Because the single-particle levels at the saddle point influence such quantities as fission-fragment angular distributions, the proper measurement and analysis of these quantities provide valuable information concerning the saddle-point shape [106].

For heavier actinide nuclei, the second saddle point decreases in height relative to the first, and these nuclei begin their descent with a shape corresponding to the first saddle point, which is reflection symmetric. In addition, the asymmetric second saddle point is only slightly lower than the corresponding symmetric one and occurs at a relatively small mass asymmetry

(for  $^{250}\text{Fm}$  these values are 1.2 MeV and 0.050, respectively, in our folded Yukawa calculations). This is at least partially responsible for the transition to symmetric divisions in the thermal-neutron-induced fission of  $^{257}\text{Fm}$ .

As the excitation energy increases, the probability for division into two equal fragments increases, until at high energies the experimental mass distribution for all nuclei is peaked about a division into two equal fragments. This transition is probably associated with the decrease in relative importance of single-particle effects at high excitation energies, where the nucleons are distributed randomly over a large number of single-particle levels. This effectively destroys the influence of the shells, and--in a loose manner of speaking--the system divides in accordance with the smooth macroscopic contribution to the energy, which prefers an equal-mass split. This will be discussed later in the symposium by Jensen [107].

The phenomena that we are able to understand qualitatively in terms of the calculated saddle-point symmetry properties are thus the mass asymmetry in the low-energy fission of most actinide nuclei, and the transitions to symmetric divisions for both lighter and heavier nuclei and at high excitation energy. The calculated saddle-point properties do not reproduce the exact locations of the transitions to symmetric divisions and do not reproduce the expected symmetric and asymmetric saddle points for nuclei such as radium in the transition region. A more quantitative study of fission-fragment mass distributions would require a dynamical calculation to determine the motion beyond the second saddle point.

## 7. CONCLUDING COMMENTS

We have discussed recent advances in the calculation of the nuclear potential energy of deformation, with primary emphasis on the macroscopic-microscopic method. As specific examples of this method we have presented some new results obtained recently at Los Alamos with the folded Yukawa and modified oscillator single-particle potentials; the macroscopic energy is calculated by use of the droplet model.

A variety of phenomena associated with nuclear shape changes can be understood on the basis of this two-part approach. The macroscopic part gives the smooth trends, and the microscopic part gives the fluctuations that arise from single-particle effects. In this way such varied phenomena as nuclear ground-state masses and deformations, second minima in the fission barriers of actinide nuclei, fission-barrier heights, and fission-fragment mass distributions are seen to have a common origin.

From comparisons with experimental results we have seen that the present accuracy with which we are able to calculate the nuclear potential energy of deformation is about 1 MeV, although larger systematic errors are still present in some cases. Some of these errors are associated with imperfect determinations of the constants of both the macroscopic energy and the single-particle potential. Numerical inaccuracies arise from calculating shell and pairing corrections for a region of nuclei from single-particle levels for one central nucleus; numerical inaccuracies are also present in the extraction of the shell correction from a given set of single-particle levels. Some of the errors could arise from an inadequate treatment of zero-point energies. Perhaps we are using the wrong functional form for either the macroscopic energy or the single-particle potential. But probably the major errors stem from an



inherent limitation of the macroscopic-microscopic method itself, such as the neglect of terms that are second order in the deviation of the actual nuclear density from a smooth density. These second-order effects will be discussed later in this session by Brack [71].

When these same general methods are applied to superheavy nuclei, we find the result shown in Fig. 18: An island of nuclei in the vicinity of 114 protons and 184 neutrons is expected to be relatively stable against spontaneous fission, alpha decay, and beta decay. As is true for any island, there are two general ways by which the island of superheavy nuclei may conceivably be reached--by sea and by air. In the next talk Howard will discuss the approach by sea, where one would reach the southeastern, or neutron-rich shore of the island through the multiple capture of neutrons [50].

---

## APPENDIX. SHAPE CONSTRAINTS

The ground-state energy is determined by minimizing the potential energy with respect to an elongation coordinate and a necking coordinate in two different shape parametrizations. We use first a constrained version of the three-quadratic-surface parametrization, which contains the six deformation coordinates  $\sigma_1, \sigma_2, \sigma_3, \alpha_1, \alpha_2,$  and  $\alpha_3$  [44-51]. The first three coordinates describe symmetric deformations, and the last three describe asymmetric deformations. For specifying ground-state deformations, we eliminate one of the three symmetric coordinates by relating the eccentricity of the middle spheroid to that of the two end spheroids. This is done by requiring that the relative quadrupole moment of the middle spheroid be equal in magnitude but of opposite sign to the relative quadrupole moment of either end spheroid. The two remaining symmetric coordinates are chosen to be the quadrupole moment  $Q_2$  and hexadecapole moment  $Q_4$  of the shape [50]. We find that this parametrization describes very poorly the shapes of nuclei with large positive hexadecapole moments (light isotopes of thorium, uranium, and plutonium). In particular, the generated shapes have a large curvature near  $z = 0$ , which results in an unphysically large surface energy. For this reason we also study the potential energy near the ground state as a function of the coordinates  $r$  and  $u_0$  in Nilsson's perturbed-spheroid parametrization [1, 2, 23-29]. For most nuclei the use of this parametrization results in a lower ground-state energy (by up to 1.2 MeV for  $^{226}\text{Th}$ ). However, for several nuclei with neutron number  $N$  close to 152 the energy calculated in the constrained version of the three-quadratic-surface parametrization is lower (by up to 0.4 MeV for  $^{250}\text{Cf}$ ). For each nucleus we use the lower ground-state energy calculated with these two parametrizations.

The remaining fission barrier extrema are determined by use of the three-quadratic-surface parametrization only. (For comparison we are currently re-determining them by use of Nilsson's perturbed-spheroid parametrization.) In this determination three coordinates are varied independently: the distance between mass centers  $r$ , the necking coordinate  $u_0$ , and the asymmetry coordinate  $\alpha_3$ . The coordinate  $\alpha_1$  is always set equal to 0, and  $\alpha_2$  is used to keep the center of mass fixed at the origin. When  $u_0$  is varied, the coordinate  $\sigma_1$  which specifies the separation of the end-spheroid centers is



determined so that the distance  $r$  between the actual nascent-fragment mass centers remains fixed. The fragment-eccentricity coordinate  $\sigma_3$  is taken equal to its value for the y-family shape [45, 47] that has the same value of  $r$ . For asymmetric shapes ( $\alpha_2 \neq 0$ ),  $r$  is chosen to be the same as for the corresponding symmetric shape. Because a large change in  $\alpha_2$  sometimes leads to a small change in the actual shape, we define the mass-asymmetry coordinate as  $(M_1 - M_2)/(M_1 + M_2) = (M_1 - M_2)/M_0$ . Here  $M_1$  is the mass on one side of the point midway between the ends of the shape, and  $M_2$  is the mass on the other side.

The asymmetric saddle points are determined in the following way: We consider seven values of  $r$  in the vicinity of the second saddle point. With  $r$  fixed we vary  $\sigma_2$  and the mass-asymmetry coordinate independently; we use five values for each of the last two coordinates, which makes a total of 25 grid points. For each mass asymmetry we minimize the energy with respect to  $\sigma_2$ . In this way we obtain for each value of  $r$  the energy as a function of mass asymmetry; these energies are then used to construct contour maps as functions of  $r$  and mass asymmetry. From these contour maps the asymmetric saddle points are then determined. In our contour maps all distortion coordinates  $(\sigma_1, \sigma_2, \sigma_3, \alpha_1, \alpha_2, \alpha_3)$  are continuous functions of  $r$  and mass asymmetry, thus insuring that we do not "tunnel through" a mountain ridge when minimizing with respect to  $\sigma_2$  and consequently obtain a spurious saddle point of lower energy.

When determining the first saddle point and second minimum, only  $r$  and  $\sigma_2$  are varied because in this region the potential energy is stable against mass-asymmetric distortions (or in a few cases only slightly unstable). Therefore, in the two contour diagrams displayed in Fig. 6 the potential energy for asymmetric shapes is minimized with respect to  $\sigma_2$  only in the vicinity of the second saddle point. In other regions asymmetric distortions are generated from the corresponding symmetric shape by making  $\alpha_2 \neq 0$ . In the region preceding the second saddle point these symmetric shapes are those for the ground state, first saddle point, and second minimum for the particular nucleus under consideration. Beyond the second saddle point the symmetric shapes correspond to those along the most probable idealized liquid-drop-model dynamical path from saddle to scission [44,51] for fissility parameter  $x \approx 0.8$ .

#### ACKNOWLEDGMENTS

Our greatest debt concerning this work is owed to our friend and colleague S. G. Nilsson, who collaborated with us in redetermining the parameters of the folded Yukawa single particle potential and who--through our near-daily interactions during the past six months--has provided new insight into most of the points discussed here. We are also grateful to R. W. Hance, W. H. Howard, M. G. Mustafa, W. D. Myers, A. J. Sienk, and W. J. Swiatecki for their contributions to this work.

# REFERENCES

- [1] LARSSON, S. E., LEANDER, G., Paper IAEA-SM-174/6, these Proceedings.
- [2] JOHANSSON, T., NILSSON, S. G., SZYMAŃSKI, Z., Ann. Phys. (Paris) 5 (1970) 377.
- [3] BRACK, M., DAMGAARD, J., JENSEN, A. S., PAULT, H. C., STRUTINSKY, V. M., WONG, C. Y., Rev. Mod. Phys. 44 (1972) 320.
- [4] NIX, J. R., Ann. Rev. Nucl. Sci. 22 (1972) 65.
- [5] PAULT, H. C., Phys. Rep. 7 (1973) 35.
- [6] BACK, B. B., BRITT, H. C., GARRETT, J. D., HANSEN, O., LEROUX, B., Paper IAEA-SM-174/201, these Proceedings; BACK, B. B., HANSEN, O., BRITT, H. C., GARRETT, J. D., Paper IAEA-SM-174/27, these Proceedings.
- [7] VANDENBOSCH, R., Paper IAEA-SM-174/203, these Proceedings.
- [8] DAVIES, K. T. K., MCCARTHY, R. J., Phys. Rev. C 4 (1971) 81.
- [9] BETHE, H. A., Ann. Rev. Nucl. Sci. 21 (1971) 93.
- [10] BASSICHIS, W. H., KERMAN, A. K., TSANG, C. F., TIERPE, D. R., WILETS, L., Magic Without Magic: John Archibald Wheeler (KLAUDER, J. R., Ed.), Freeman, San Francisco (1972) 15.
- [11] BASSICHIS, W. H., KERMAN, A. K., Phys. Rev. C 6 (1972) 370.
- [12] KERMAN, A. K., PAL, M. K., Phys. Rev. 162 (1967) 970.
- [13] MELDNER, H. W., Phys. Rev. 178 (1969) 1815.
- [14] KÖHLER, H. S., Nucl. Phys. A170 (1971) 88.
- [15] SKYRME, T. H. R., Nucl. Phys. 9 (1959) 615.
- [16] VAUTHERIN, D., BRINK, D. H., Phys. Rev. C 5 (1972) 626.
- [17] FLOCARD, H., QUENTIN, P., KERMAN, A. K., VAUTHERIN, D., Nucl. Phys. A203 (1973) 433.
- [18] QUENTIN, P., Orsay Preprint (1973).
- [19] FLOCARD, H., QUENTIN, P., VAUTHERIN, D., KERMAN, A. K., Paper IAEA-SM-174/38, these Proceedings.
- [20] BRITT, H. C., BOLSTERLI, H., NIX, J. R., NORTON, J. L., Phys. Rev. C 7 (1973) 801.
- [21] STRUTINSKY, V. M., Yad. Fiz. 3 (1966) 614; Sov. J. Nucl. Phys. 3 (1966) 449.
- [22] SWIATECKI, W. J., Nuclidic Masses (Proc. Conf. Vienna, 1963), Springer-Verlag (1964) 58.
- [23] GUSTAFSSON, C., LAMM, I. L., NILSSON, B., NILSSON, S. G., Ark. Fys. 36 (1967) 613.
- [24] NILSSON, S. G., TSANG, C. F., SOBIECHOWSKI, A., SZYMAŃSKI, Z., WYCECH, S., GUSTAFSSON, C., LAMM, I. L., MÖLLER, P., NILSSON, B., Nucl. Phys. A131 (1969) 1.
- [25] TSANG, C. F., NILSSON, S. G., Nucl. Phys. A140 (1970) 289.
- [26] MÖLLER, P., NILSSON, S. G., Phys. Lett. 31B (1970) 283.
- [27] GUSTAFSSON, C., MÖLLER, P., NILSSON, S. G., Phys. Lett. 34B (1971) 349.
- [28] MÖLLER, P., Nucl. Phys. A192 (1972) 529.
- [29] SFLGER, P. A., Atomic Masses and Fundamental Constants (Proc. Conf. Teddington, 1971), Plenum, London (1972) 255.
- [30] LARSEN, J. N. P., Phys. Rev. 139 (1965) B1227.
- [31] HASSE, R. W., Nucl. Phys. A128 (1969) 609.
- [32] STRUTINSKY, V. M., PAULT, H. C., Physics and Chemistry of Fusion (Proc. Symp. Vienna, 1969), IAEA, Vienna (1969) 155.
- [33] PAULT, H. C., LEDERGERBER, T., BRACK, M., Phys. Lett. 34B (1971) 264.
- [34] PAULT, H. C., LEDERGERBER, T., Nucl. Phys. A175 (1971) 545.
- [35] PAULT, H. C., LEDERGERBER, T., Paper IAEA-SM-174/206, these Proceedings.
- [36] ADELY, G. D., GADALYA, I. A., CHERDANTSEV, P. A., Yad. Fiz. 13 (1971) 1180; Sov. J. Nucl. Phys. 13 (1971) 679.

- [37] PASHKEVICH, V. V., Nucl. Phys. A169 (1971) 275.
- [38] NIX, J. R., SWIATECKI, W. J., Nucl. Phys. 71 (1965) 1.
- [39] MARUIN, J., GREINER, W., Z. Phys. 251 (1972) 431.
- [40] MARUIN, J., GREINER, W., Paper IAEA-SM-174/102, these Proceedings.
- [41] MOSEL, U., Phys. Rev. C 6 (1972) 971.
- [42] MUSTAFA, M. G., MOSEL, U., SCIMITT, H. W., Phys. Rev. C 7 (1973) 1519.
- [43] MUSTAFA, M. G., SCIMITT, H. W., Oak Ridge Preprint (1973).
- [44] NIX, J. R., Nucl. Phys. A130 (1969) 241.
- [45] BOLSTERLI, M., FISET, E. O., NIX, J. R., Physics and Chemistry of Fission (Proc. Symp. Vienna, 1969), IAEA, Vienna (1969) 183.
- [46] FISET, E. O., NIX, J. R., BOLSTERLI, M., Los Alamos Rep. LA-4735-MS (1971).
- [47] BOLSTERLI, M., FISET, E. O., NIX, J. R., NORTON, J. L., Phys. Rev. C 5 (1972) 1050.
- [48] FISET, E. O., NIX, J. R., Nucl. Phys. A193 (1972) 647.
- [49] NIX, J. R., Warsaw Rep. INR-P-1447/I/PL (1972) 299.
- [50] HOWARD, W. M., NIX, J. R., Paper IAEA-SM-174/60, these Proceedings.
- [51] SIERK, A. J., NIX, J. R., Paper IAEA-SM-174/74, these Proceedings.
- [52] ANDERSEN, B. L., DICKMANN, F., DIETRICH, K., Nucl. Phys. A159 (1970) 337.
- [53] KOONIN, S. E., unpublished (1972).
- [54] MYERS, W. D., SWIATECKI, W. J., Ann. Phys. (New York) 55 (1969) 395.
- [55] MYERS, W. D., SWIATECKI, W. J., Berkeley Rep. UCRL-19543 (1970).
- [56] MYERS, W. D., SWIATECKI, W. J., Berkeley Preprint LBL-1957 (1973).
- [57] MYERS, W. D., SWIATECKI, W. J., Ark. Fys. 36 (1967) 343.
- [58] BETHE, H. A., Phys. Rev. 167 (1968) 879.
- [59] BRUECKNER, K. A., BUCHLER, J. R., CLARK, R. C., LOMBARD, R. J., Phys. Rev. 181 (1969) 1543.
- [60] BRUECKNER, K. A., CLARK, R. C., LTN, W., LOMBARD, R. J., Phys. Rev. C 1 (1970) 249.
- [61] BRUECKNER, K. A., BUCHLER, J. R., KELLY, M. H., Phys. Rev. 173 (1968) 944.
- [62] SCHEID, W., GREINER, W., Z. Phys. 226 (1969) 364.
- [63] KRAPPE, H. J., NIX, J. R., Paper IAEA-SM-174/12, these Proceedings.
- [64] NILSSON, S. G., NIX, J. R., MÖLLER, P., Los Alamos Preprint (1973).
- [65] STRUTINSKY, V. M., Nucl. Phys. A122 (1968) 1.
- [66] PASHKEVICH, V. V., Nucl. Phys. A133 (1969) 400.
- [67] NILSSON, S. G., private communication (1973).
- [68] GÖTZ, U., PAULI, H. G., JUNKER, K., Phys. Lett. 39B (1972) 436.
- [69] MYERS, W. D., Nucl. Phys. A145 (1970) 387.
- [70] GEILIKMAN, B. T., Yad. Fiz. 9 (1969) 894; Sov. J. Nucl. Phys. 9 (1969) 521.
- [71] BRACK, M., QUENTIN, P., Paper IAEA-SM-174/98, these Proceedings.
- [72] BUNATIAN, G. G., KOLOMIETZ, V. M., STRUTINSKY, V. M., Nucl. Phys. A188 (1972) 225.
- [73] RAMAMURTHY, V. S., KAPOOR, S. S., Phys. Lett. 42B (1972) 399.
- [74] RAMAMURTHY, V. S., KAPOOR, S. S., Abstract, these Proceedings.
- [75] RAMAMURTHY, V. S., KAPOOR, S. S., Int. Conf. Nuclear Physics (Proc. Conf. Munich, 1973) 1, North-Holland, Amsterdam (1973).
- [76] WILLIAMS, F. G., Jr., CHAN, G., HUIZENGA, J. R., Nucl. Phys. A187 (1972) 225.
- [77] BENGTSSON, R., Nucl. Phys. A198 (1972) 591.
- [78] JAMES, G. D., LYNN, J. E., FARWELL, L. G., Nucl. Phys. A189 (1972) 225.
- [79] BACK, B. B., BRITT, H. C., CARRIET, J. D., HANSEN, O., Phys. Rev. Lett. 28 (1972) 1707.
- [80] RASBUP, J., TSANG, C. P., MÖLLER, P., NILSSON, S. G., LARSSON, S. E., Berkeley Preprint (1973).

- [81] RANDRUP, J., Abstract, these Proceedings.
- [82] WILETS, L., Theories of Nuclear Fission, Clarendon, Oxford (1964) 46.
- [83] WAPSTRA, A. H., COVE, N. B., Nucl. Data Tables 9 (1971) 265.
- [84] BJØRNHOLM, S., LYNN, J. E., unpublished (1970).
- [85] RUSSO, P. A., PEDERSEN, J., VANDENBOSCH, R., Paper IAEA-SM-174/96, these Proceedings.
- [86] BENGTSSON, R., Paper IAEA-SM-174/7, these Proceedings.
- [87] MORETTO, L. G., THOMPSON, S. G., ROUTTI, J., GATTI, R. C., Phys. Lett. 38B (1972) 471.
- [88] HULET, E. K., WILD, J. P., LOUGHEED, R. W., EVANS, J. E., QUALHEIM, B. J., NURMIA, M., GHIORSO, A., Phys. Rev. Lett. 26 (1971) 523.
- [89] PHILLIPS, L., GATTI, R. C., CHESNE, A., MUGA, L., THOMPSON, S. G., Phys. Rev. Lett. 1 (1958) 215.
- [90] NURMIA, M., SIKKELAND, T., SILVA, R., GHIORSO, A., Phys. Lett. 26B (1967) 78.
- [91] BALIAN, R., BLOCH, C., Ann. Phys. (New York) 69 (1972) 76.
- [92] SPECHT, H. J., WEBER, J., KONECNY, E., HEUNEMANN, D., Phys. Lett. 41B (1972) 43.
- [93] SOBICZENSKI, A., BJØRNHOLM, S., POMORSKI, K., Nucl. Phys. A202 (1973) 274.
- [94] VANDENBOSCH, R., RUSSO, P. A., SLETTEN, G., MEHTA, M., Seattle Preprint (1973).
- [95] BUSINARO, U. I., GALLONE, S., Nuovo Cim. 5 (1957) 315.
- [96] SWIATECKI, W. J., unpublished (1969).
- [97] ANDERSEN, B. L., Phys. Lett. 42B (1972) 307.
- [98] VON GUNTEN, H. R., Actinides Rev. 1 (1969) 275.
- [99] HOFFMAN, D. C., Los Alamos Rep. LA-DC-72-898 (1972).
- [100] BRANDT, R., THOMPSON, S. G., GATTI, R. C., PHILLIPS, L., Phys. Rev. 131 (1963) 2617.
- [101] TSANG, C. F., WILHELMY, J. B., Nucl. Phys. A184 (1972) 417.
- [102] BALAGNA, J. P., FORD, G. P., HOFFMAN, D. C., KNIGHT, J. D., Phys. Rev. Lett. 26 (1971) 145.
- [103] JOHN, W., HULET, E. K., LOUGHEED, R. W., WESOLOWSKI, J. J., Phys. Rev. Lett. 27 (1971) 45.
- [104] KONECNY, E., SPECHT, H. J., WEBER, J., Munich Preprint (1973).
- [105] KONECNY, E., SPECHT, H. J., WEBER, J., Paper IAEA-SM-174/20, these Proceedings.
- [106] FREILEBEN, H., BRITT, H. C., HUIZENGA, J. R., Paper IAEA-SM-174/56, these Proceedings.
- [107] JENSEN, A. S., DOSSING, T., Paper IAEA-SM-174/28, these Proceedings.

## FIGURE CAPTIONS

- FIG. 1. Effect of axial asymmetry and mass asymmetry on the fission barrier of  $^{240}\text{Pu}$ . The dashed curve (which sometimes coincides with the solid curve) gives the potential energy for symmetric deformations as a function of the distance  $r$  between the centers of mass of the two nascent fragments. The solid curve gives the potential energy along a path that leads over the axially asymmetric first saddle point and over the mass-asymmetric second saddle point. The lower portion of the figure shows the nuclear shapes corresponding to selected points along this path, namely the sphere, four equilibrium points, and the point of emergence from the barrier in spontaneous fission. The results for axially symmetric shapes are calculated with the folded Yukawa potential and the droplet model by use of methods to be described later. The reduction in energy at the first saddle point is taken from Ref. [1].
- FIG. 2. Nuclear shapes described by the fission coordinate  $y$ , and the corresponding spin-independent nuclear single-particle potentials for a diffuse-surface folded Yukawa potential [45, 47, 49]. The equipotential curves are shown for 10, 30, 50, 70, and 90% of the well depth.
- FIG. 3. Energy levels of a harmonic-oscillator potential for prolate spheroidal deformations [49]. The particle numbers of the closed shells are indicated for a sphere and for a spheroid whose major axis is twice its minor axis.
- FIG. 4. Extraction of the shell correction from single-particle energies [47, 49]. The neutron levels in a spherical  $^{200}\text{Pb}$  nucleus are shown by solid points and define a staircase function  $\epsilon_{\text{stair}}(n)$ . The smooth curve  $\bar{\epsilon}(n)$  removes the local fluctuations of the solid points but retains their long-range behavior. The Fermi surface  $\bar{\lambda}$  of the smooth distribution of levels is illustrated for 126 neutrons. The corresponding shell correction is given by the difference between the areas under the staircase curve and the smooth curve up to  $n = 126$ .
- FIG. 5. Fission barriers for actinide nuclei, calculated with the folded Yukawa potential and the droplet model. The dashed curves (which sometimes coincide with the solid curves) give the potential energy for symmetric deformations as a function of the distance  $r$  between the centers of mass of the two nascent fragments. The solid curves give the potential energy along a path that leads over the mass-asymmetric second saddle point. This path is usually determined by minimizing the potential energy with respect to mass asymmetry for fixed values of  $r$ . However, when such a path jumps discontinuously from one valley to another without passing over the asymmetric saddle point, the path in this region is determined by the method of steepest descent. This explains why the solid curves sometimes lie above the dashed curves. The potential energy for each nucleus is calculated with single-particle levels for  $^{240}\text{Gf}$ .

FIG. 6. Potential energy of  $^{236}\text{U}$  and  $^{250}\text{Pm}$ , calculated with the folded Yukawa potential and the droplet model. For each nucleus contours of constant potential energy are plotted as functions of the distance between mass centers  $r$  and the mass-asymmetry coordinate  $(M_1 - M_2)/M_0$ . The contours are labelled by the energy (in MeV) relative to the spherical droplet-model energy. The solid curves are spaced at intervals of 2 MeV; dashed curves are used for intermediate values. The distortions included vary from a sphere (at  $r = 0.75 R_0$ ) all the way to scission, which is indicated by the slightly curved dot-dashed line. The potential energy for each nucleus is calculated with single-particle levels for  $^{250}\text{Cf}$ .

FIG. 7. Potential energy of  $^{236}\text{U}$ , calculated by Mustafa, Mosel, and Schmitt with a modified two-center oscillator potential [42]. Contours of constant potential energy are plotted as functions of the neck radius  $D$  and the masses of the two nascent fragments. The contours are spaced at intervals of 1 MeV and are labelled by the energy (in MeV) relative to the ground-state minimum potential energy; an additional contour is included near each saddle point. The dashed lines represent interpolated or extrapolated values.

FIG. 8. Comparison of the folded Yukawa potential with the two-center oscillator potential at the asymmetric second saddle point for  $^{236}\text{U}$ . The upper portion of the figure shows the saddle-point shapes, and the lower portion shows the corresponding potentials along the symmetry axis. The folded Yukawa potential is 0.19 MeV higher in the neck than in the center of the larger nascent fragment and is 0.04 MeV higher in the neck than in the center of the smaller nascent fragment. The two-center oscillator potential [42] is 5 MeV higher in the middle than in the center of either nascent fragment.

FIG. 9. Comparison of experimental ground-state single-particle corrections for even nuclei with values calculated by use of the folded Yukawa potential and the droplet model. The ground-state single-particle correction is the nuclear ground-state mass relative to the spherical macroscopic energy, which is calculated here from the 1973 droplet model of Myers and Swiatecki [50, 55, 56]. The experimental masses are taken from Ref. [83]. The calculated masses are obtained by minimizing the potential energy with respect to a separation coordinate and a necking coordinate in two different shape parametrizations, as discussed in the appendix. Single-particle levels for  $^{200}\text{Pb}$ ,  $^{224}\text{Ra}$ , and  $^{250}\text{Cf}$  are used to calculate the potential energy for each nucleus in the left-hand, middle, and right-hand regions, respectively; these regions are indicated by the dashed vertical lines. A constant ground-state zero-point energy of 0.5 MeV is included for each nucleus. The lower portion of the figure gives the discrepancy between the experimental and calculated masses.

FIG. 10. Heights of the first saddle point, second minimum, and asymmetric second saddle point, as functions of neutron number  $N$ . The solid curves give the heights calculated with the folded Yukawa potential and the droplet model relative to the calculated ground-state energy, and the dashed curves give the corresponding height relative to the experimental ground-state energy. The lightweight dot-dashed lines in the first column give the height of the lower of the two asymmetric saddle points that surround the asymmetric third minimum.

(relative to the calculated ground-state energy). To the left of the wavy vertical line the lower saddle point occurs before the minimum, and to the right it occurs after the minimum. The height of this third minimum is given in the second column by the lightweight dot-dashed lines. A constant zero-point energy of 0.5 MeV is included for each nucleus at its ground state, second minimum, and third minimum. The potential energy for each nucleus is calculated with single-particle levels for  $^{250}\text{Cf}$ . The calculations are performed for even nuclei only, but odd-neutron nuclei are also included in the experimental data, which are given by solid circles [20], open circles [84], solid squares [79], open squares [78], solid upward-pointing triangles [6], and a solid downward-pointing triangle [85].

FIG. 11. Reduction in the height of the first saddle point due to axially asymmetric deformations, as a function of mass number  $A$ . The open circles connected by the dashed lines give the heights calculated with a modified oscillator potential and the liquid-drop model for shapes that are restricted to axial symmetry [28]; the open circles connected by the solid lines give the corresponding heights calculated by Larsson and Leander for axially asymmetric shapes [1]. The strength of the pairing interaction is assumed to be proportional to the surface area; the liquid-drop-model constants are taken from Ref. [57]. No zero-point energy is included at the ground state. The calculations are performed for even nuclei only, but odd-neutron nuclei are also included in the experimental data, which are given by the solid squares [84].

FIG. 12. Height of the second minimum, as a function of neutron number  $N$ . The curves are calculated with the modified oscillator potential and the droplet model for even nuclei. The experimental data are given by circles [20] and a triangle [85]. Solid symbols are used for even nuclei, and open symbols are used for odd-neutron nuclei.

FIG. 13. Height of the asymmetric second saddle point, as a function of neutron number  $N$ . The curves are calculated with the modified oscillator potential and the droplet model for even nuclei. A constant ground-state zero-point energy of 0.5 MeV is included for each nucleus. The experimental data are given by squares [84], circles [20], and triangles [6]. Solid symbols are used for even nuclei, and open symbols are used for odd-neutron nuclei.

FIG. 14. Square of the frequency of mass-asymmetric oscillations of an idealized liquid drop about its saddle-point shape, as a function of flexibility parameter  $x$ . The results are shown for nuclei along the valley of beta stability [44]. The critical Bechnaro-Gallone point [95] is denoted by the arrow. To the right of this point the liquid-drop-model saddle-point shape is stable against mass asymmetry, and to the left it is unstable.

FIG. 15. Single-neutron levels near the second saddle point of an actinide nucleus, as functions of the mass-asymmetry coordinate  $\epsilon_{33}$ . The levels are calculated with the modified oscillator potential for asymmetric distortions defined by  $\epsilon_{33} = \epsilon_{33}$  and  $\epsilon_{33} = 0.45 \epsilon_{33}$  [27]. The levels are labelled by the asymptotic quantum numbers  $[N_2 A_2]$  and by the parity for the corresponding symmetric shape.

- FIG. 16. Correlation of experimental most probable fission-fragment mass asymmetries with values calculated at the asymmetric second saddle point by use of the folded Yukawa potential and the droplet model, for even actinide compound nuclei. The experimental data are given by circles [98], triangles [99], and squares [100]. Solid symbols are used for spontaneous fission, and open symbols are used for neutron-induced fission.
- FIG. 17. Correlation of the peak-to-valley ratio in experimental fission-fragment mass distributions with the difference between the energies of the symmetric and asymmetric second saddle points, for even actinide compound nuclei. The energy differences are calculated with the folded Yukawa potential and the droplet model. The experimental data are given by circles [98] and triangles [99]. Solid symbols are used for spontaneous fission, and open symbols are used for neutron-induced fission.
- FIG. 18. Location of the predicted island of superheavy nuclei relative to the peninsula of observed nuclei. The nuclei included in the island have calculated total halflives longer than about 5 min [48].



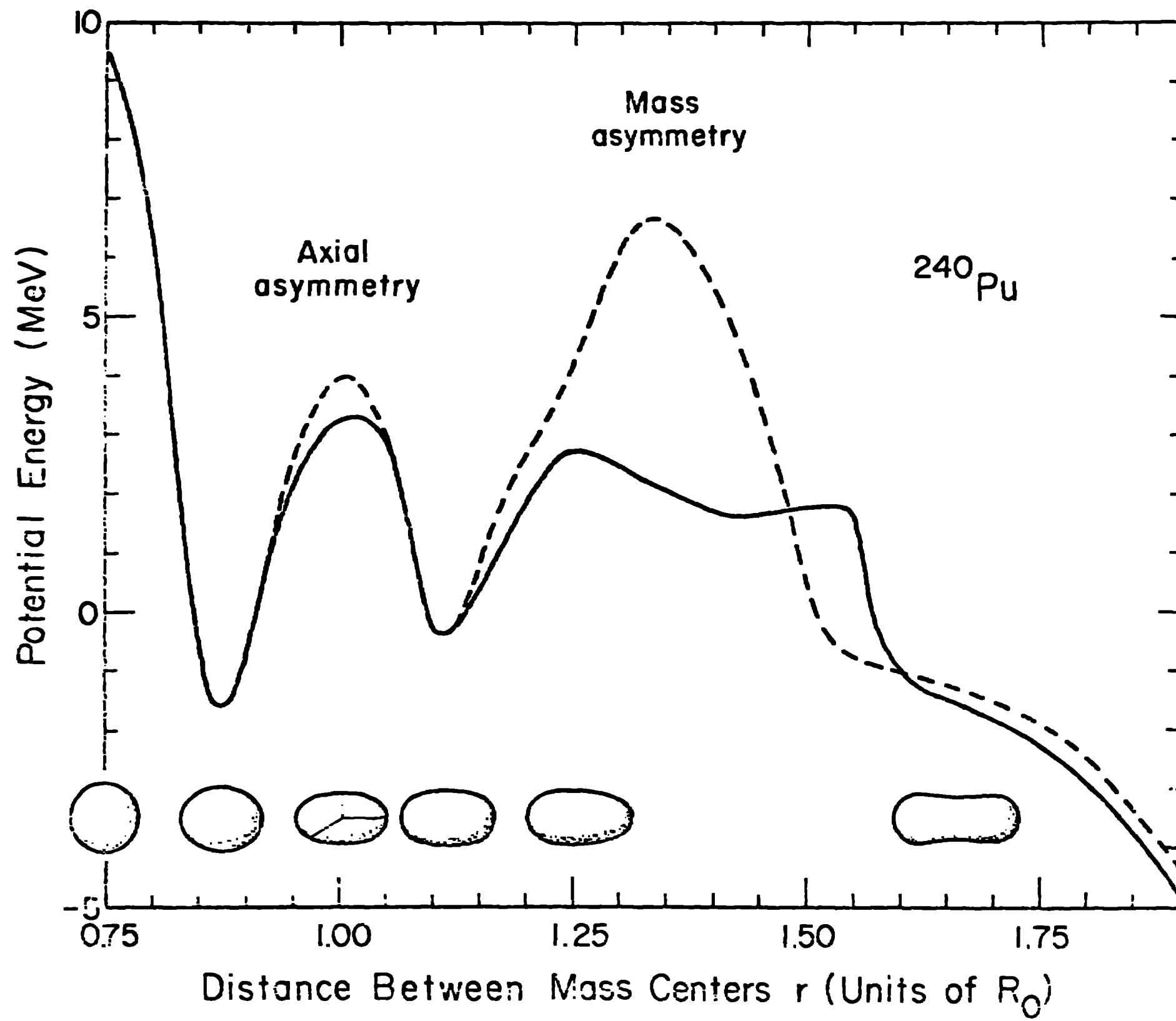


Figure 1

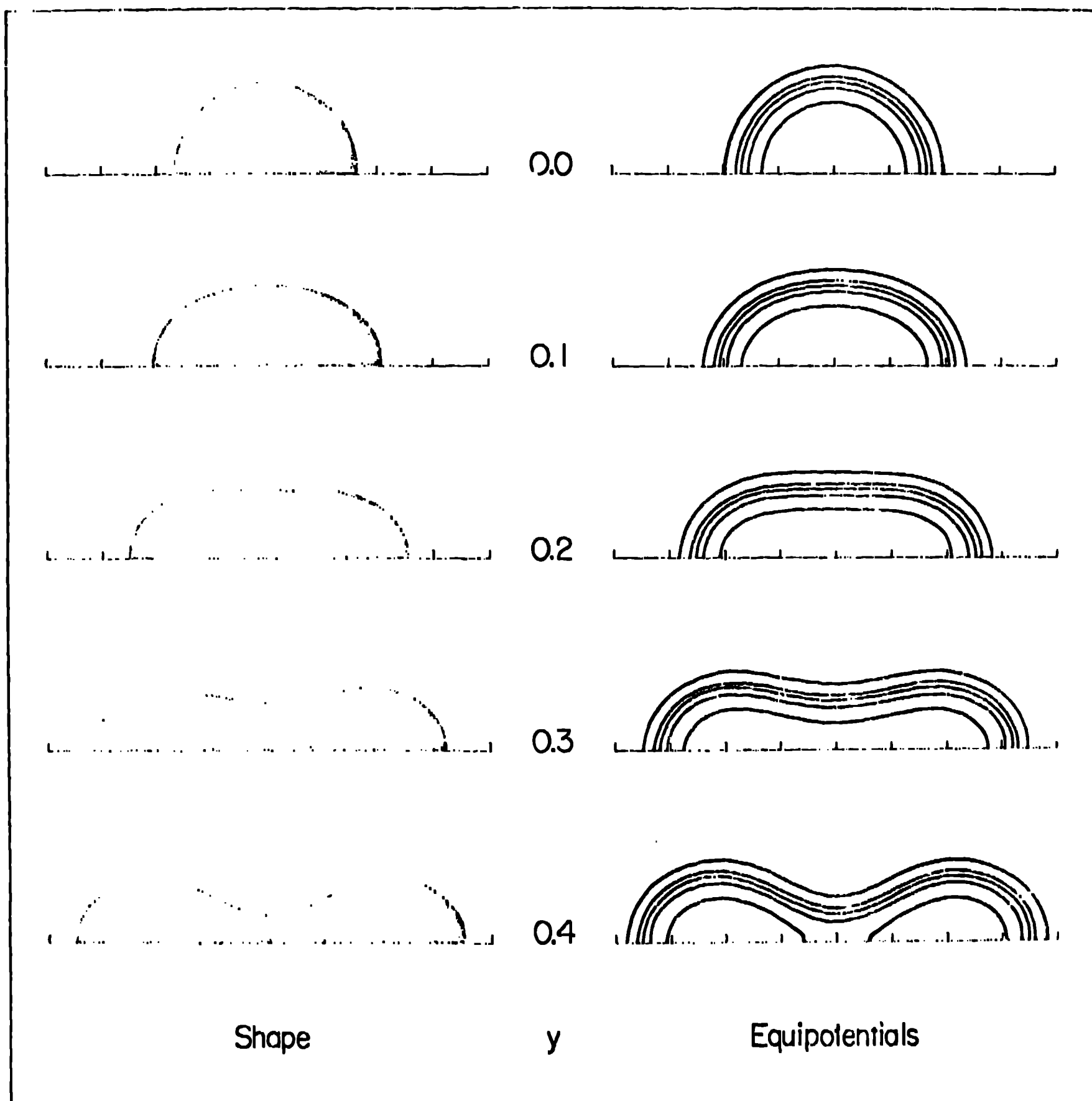


Figure 2

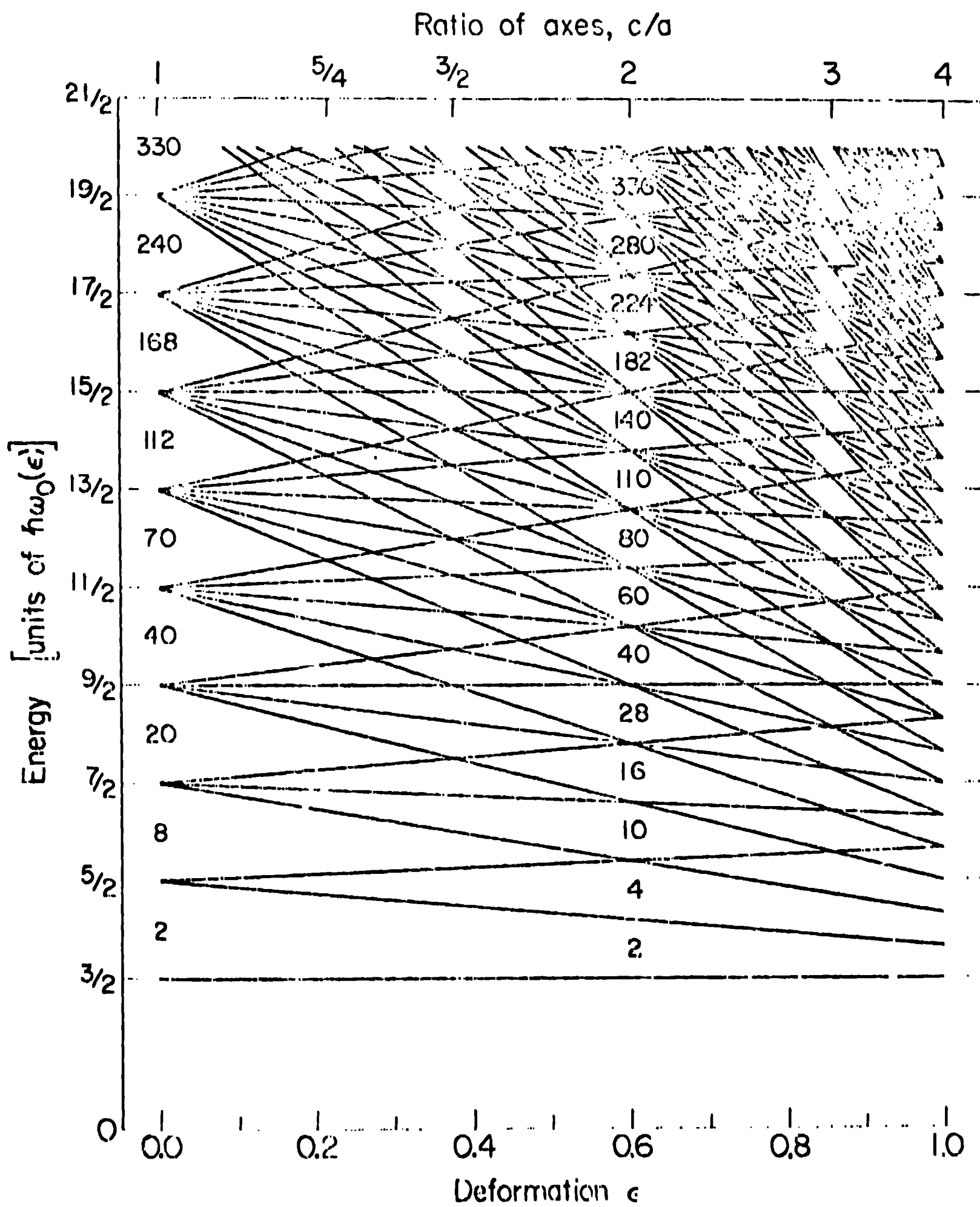


Figure 3

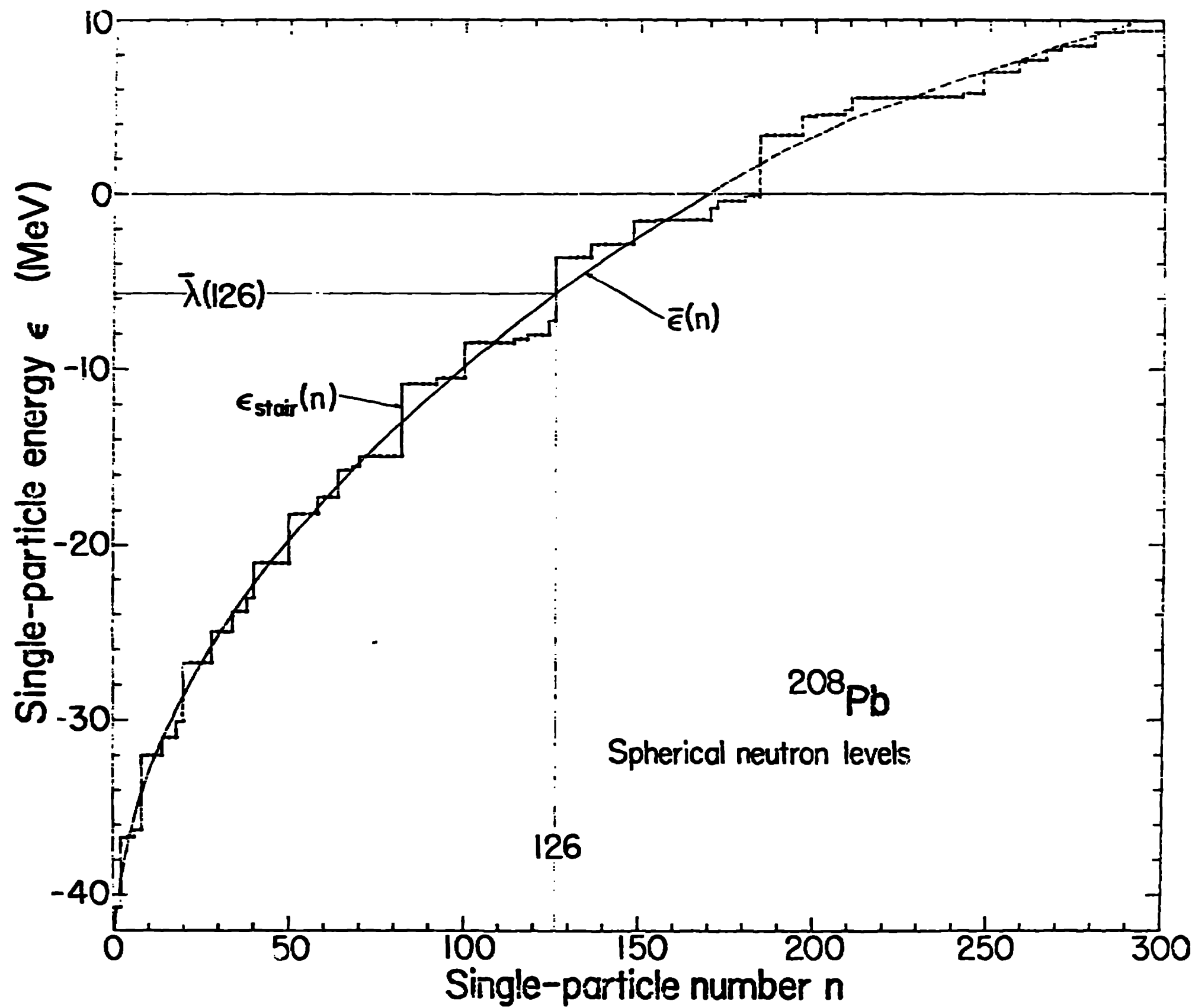


Figure 4

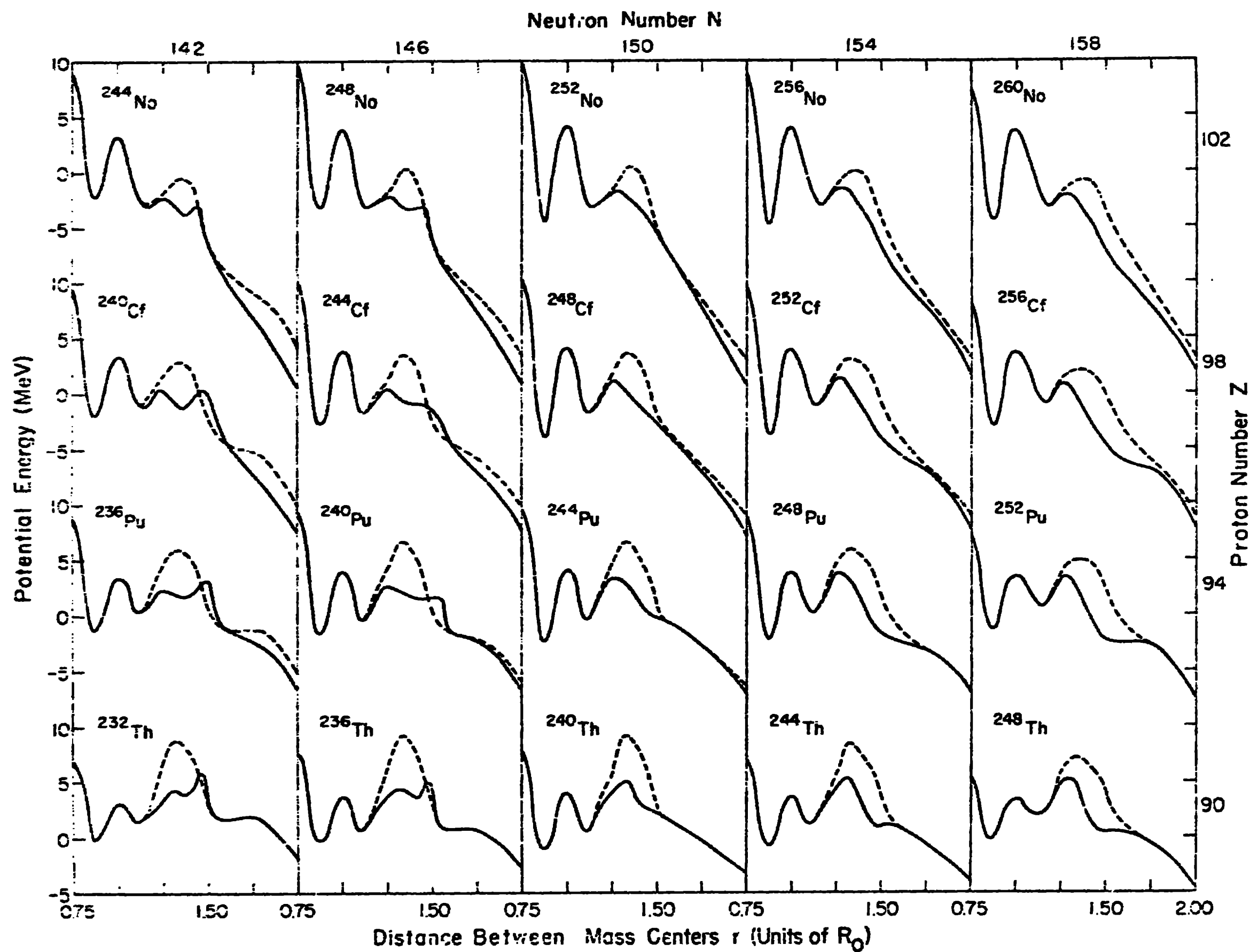


Figure 5

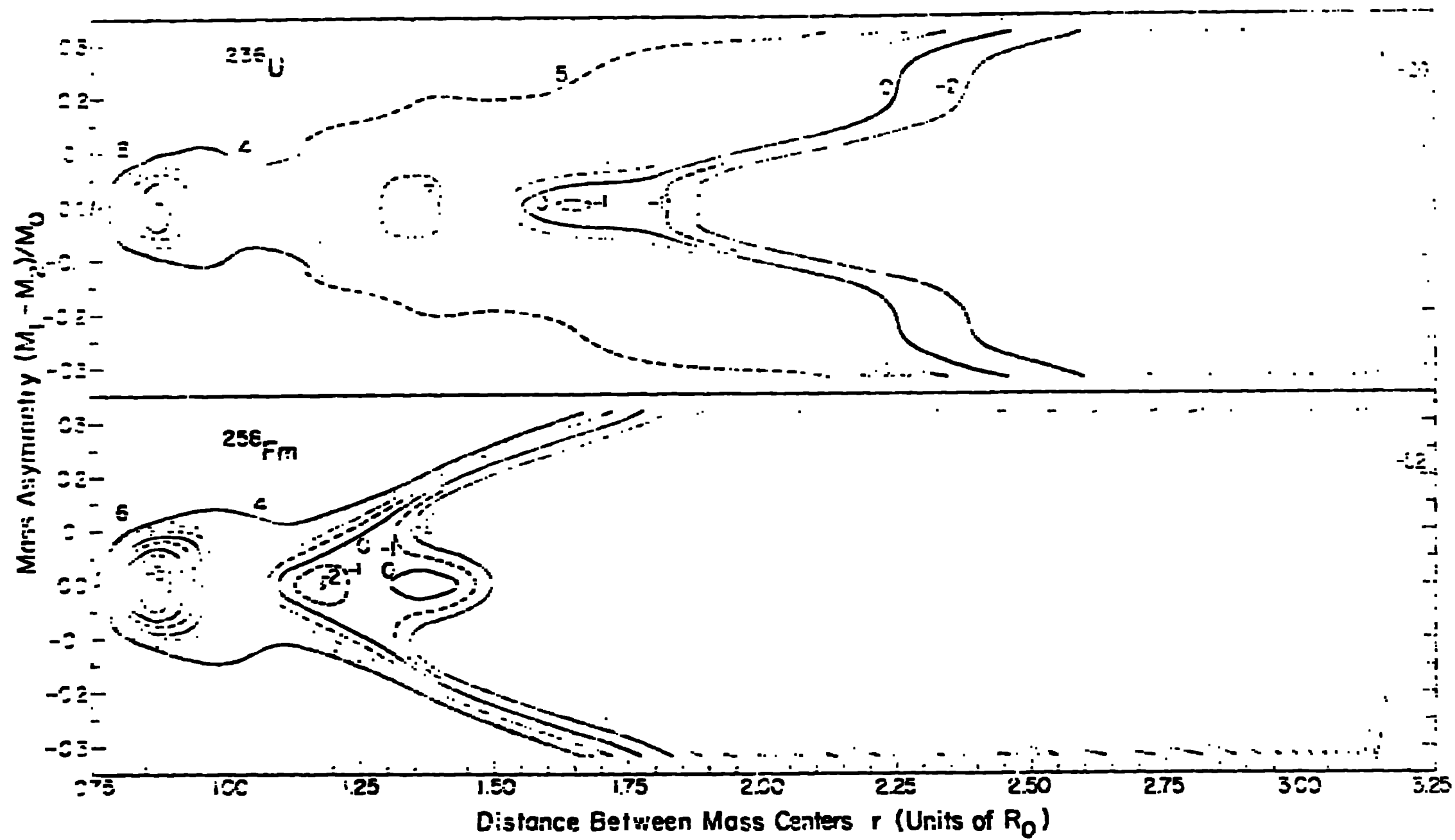
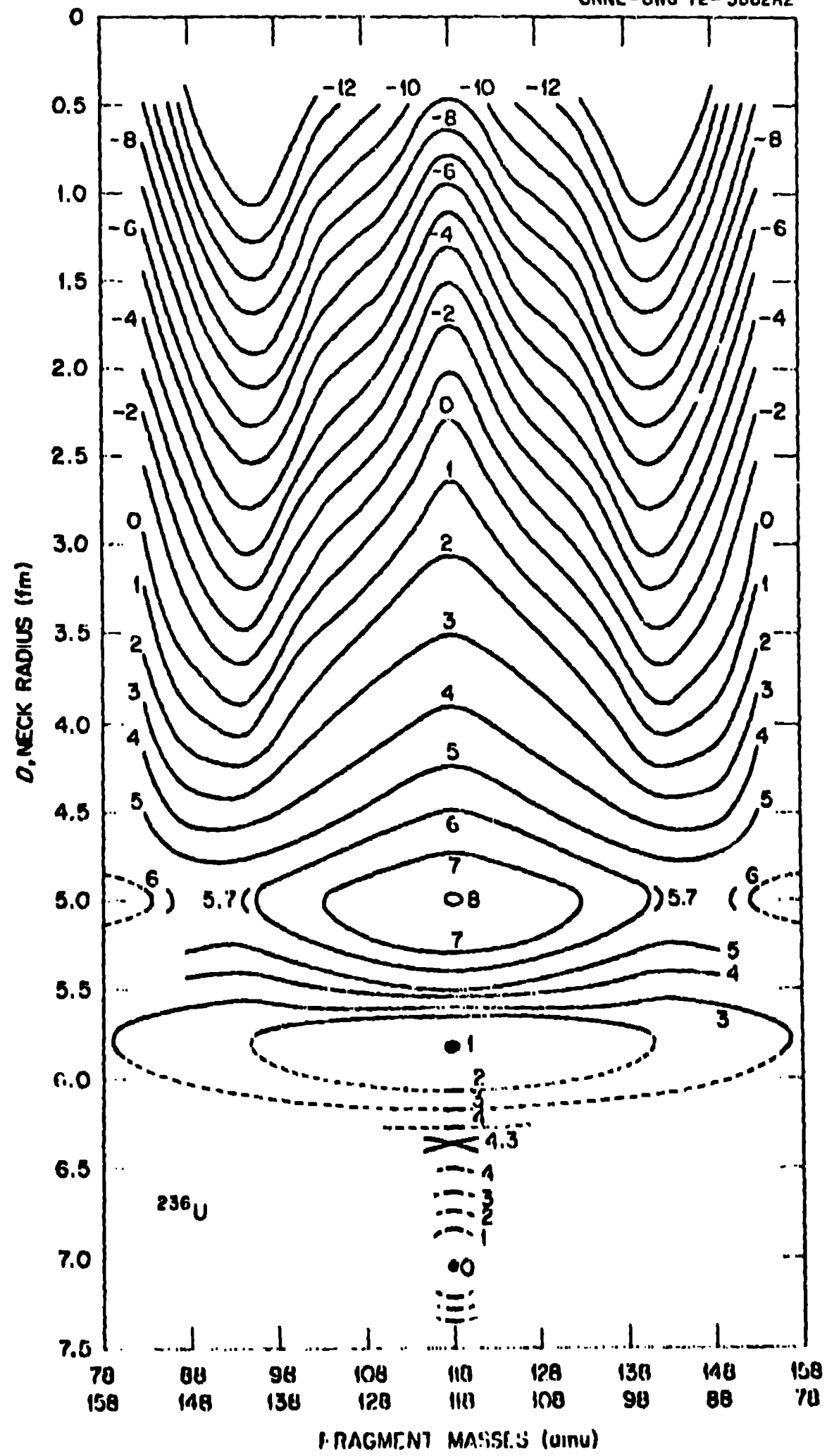


Figure 6



Potential Energy Surface for the Fission of  $^{236}\text{U}$ .

Figure 7

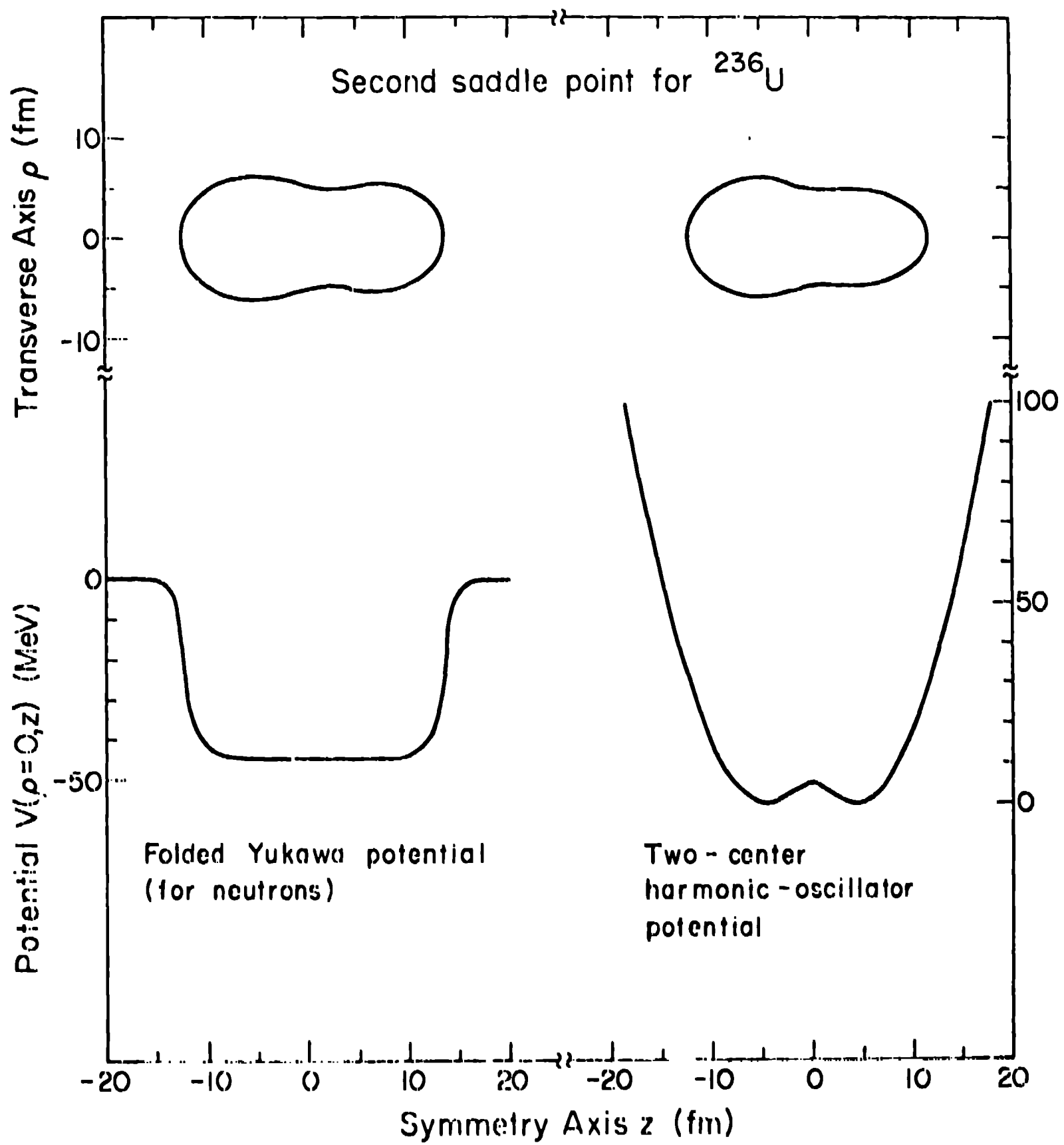


Figure 8



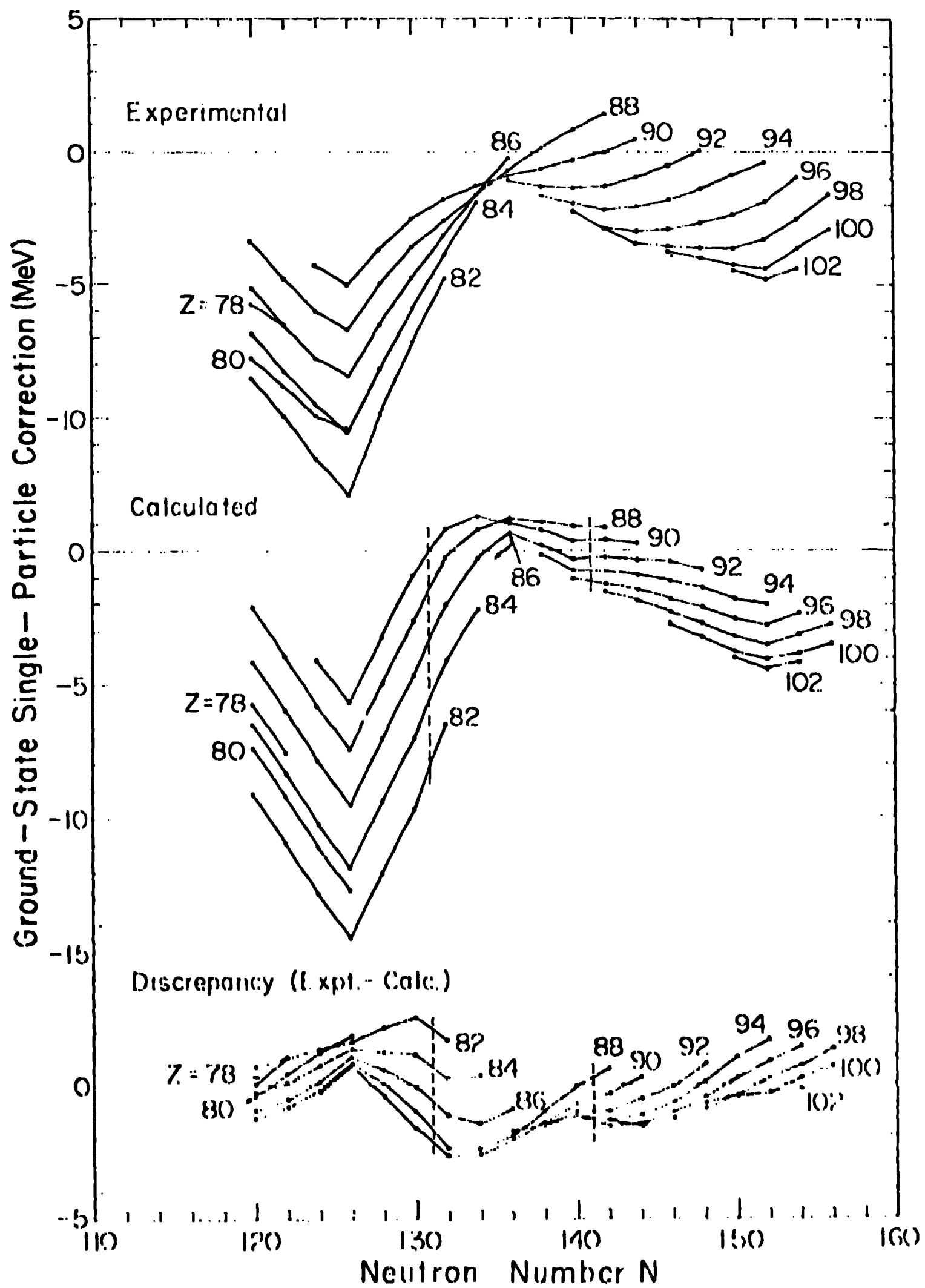


Figure 9

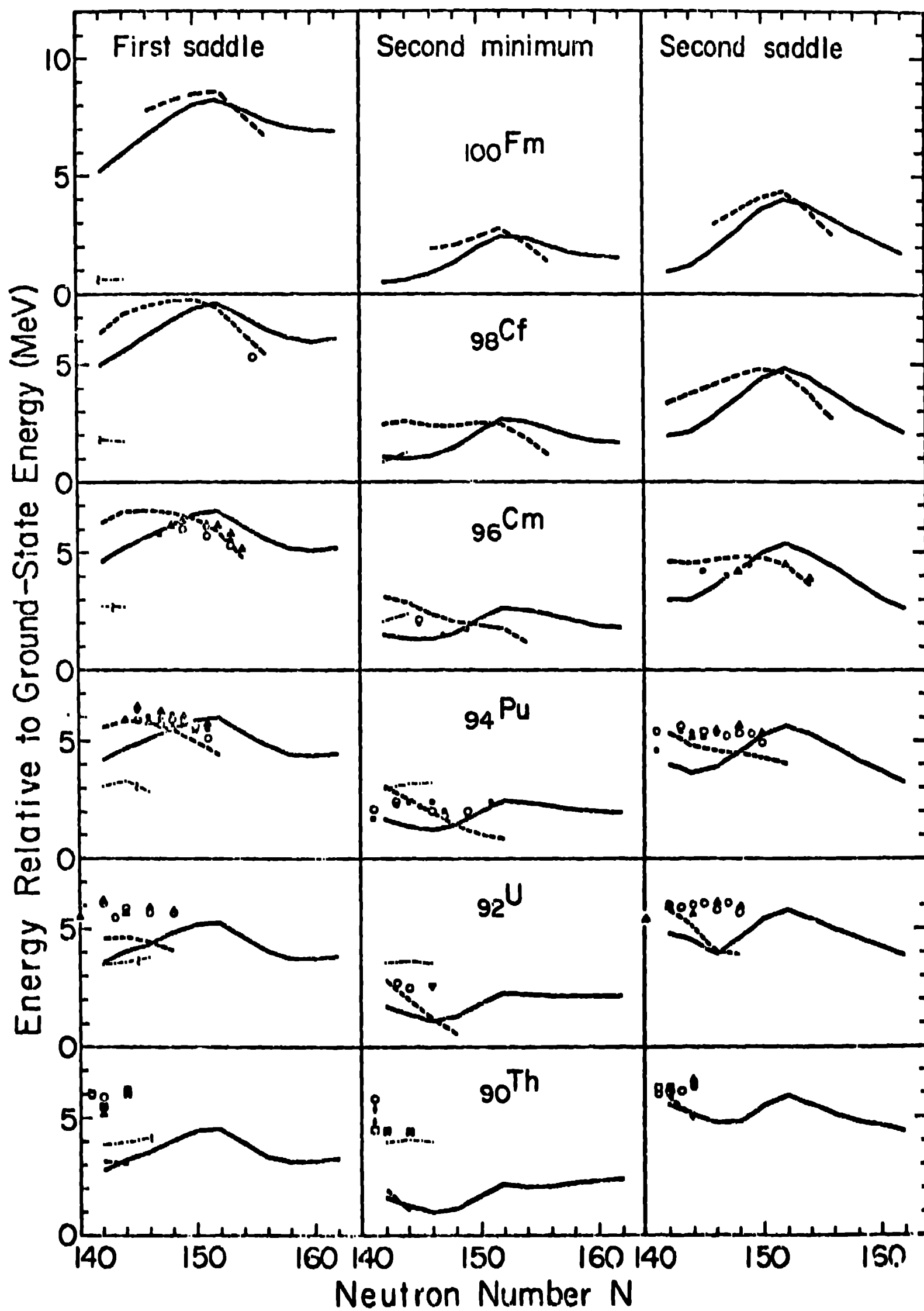


Figure 10

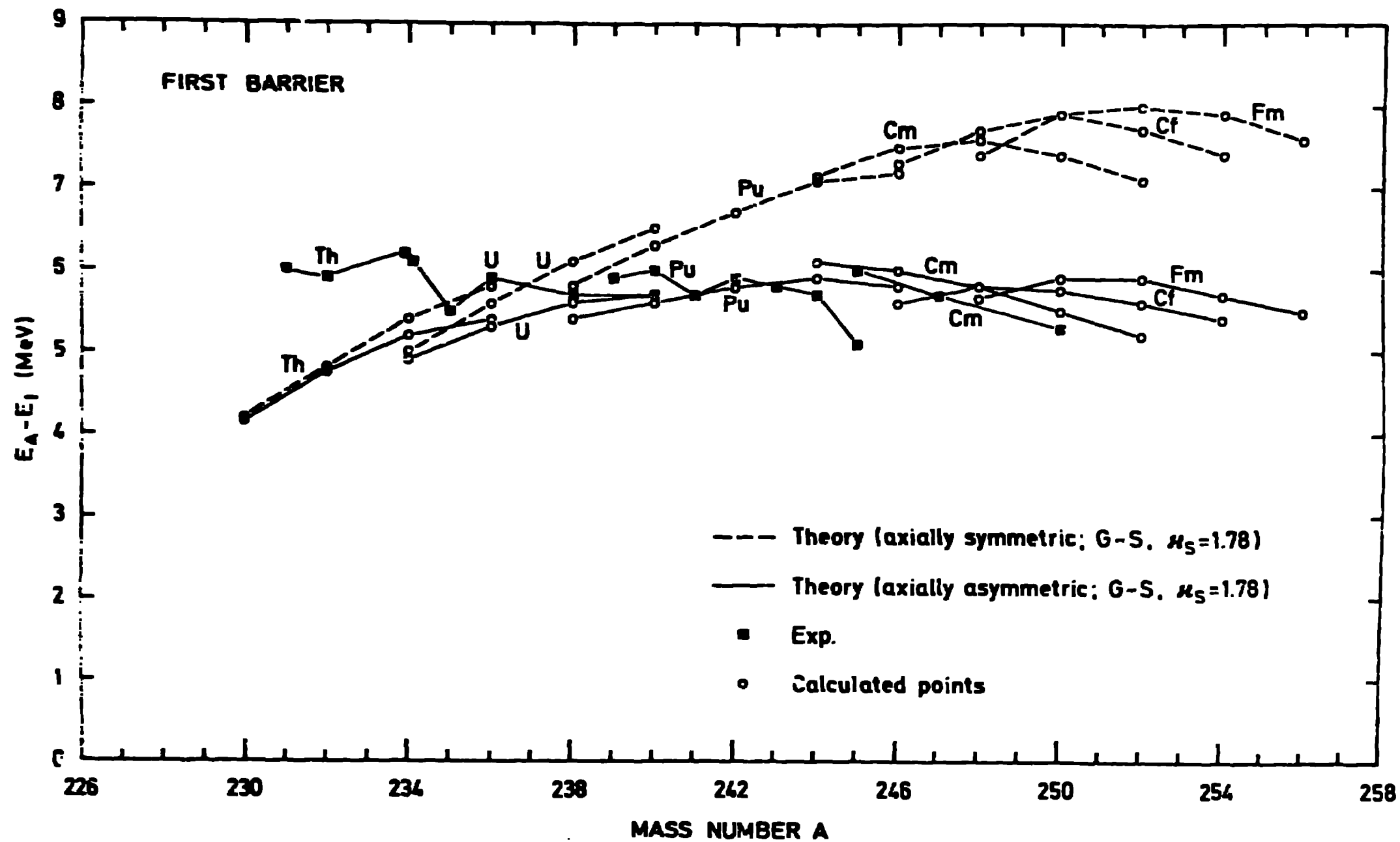


Figure 11

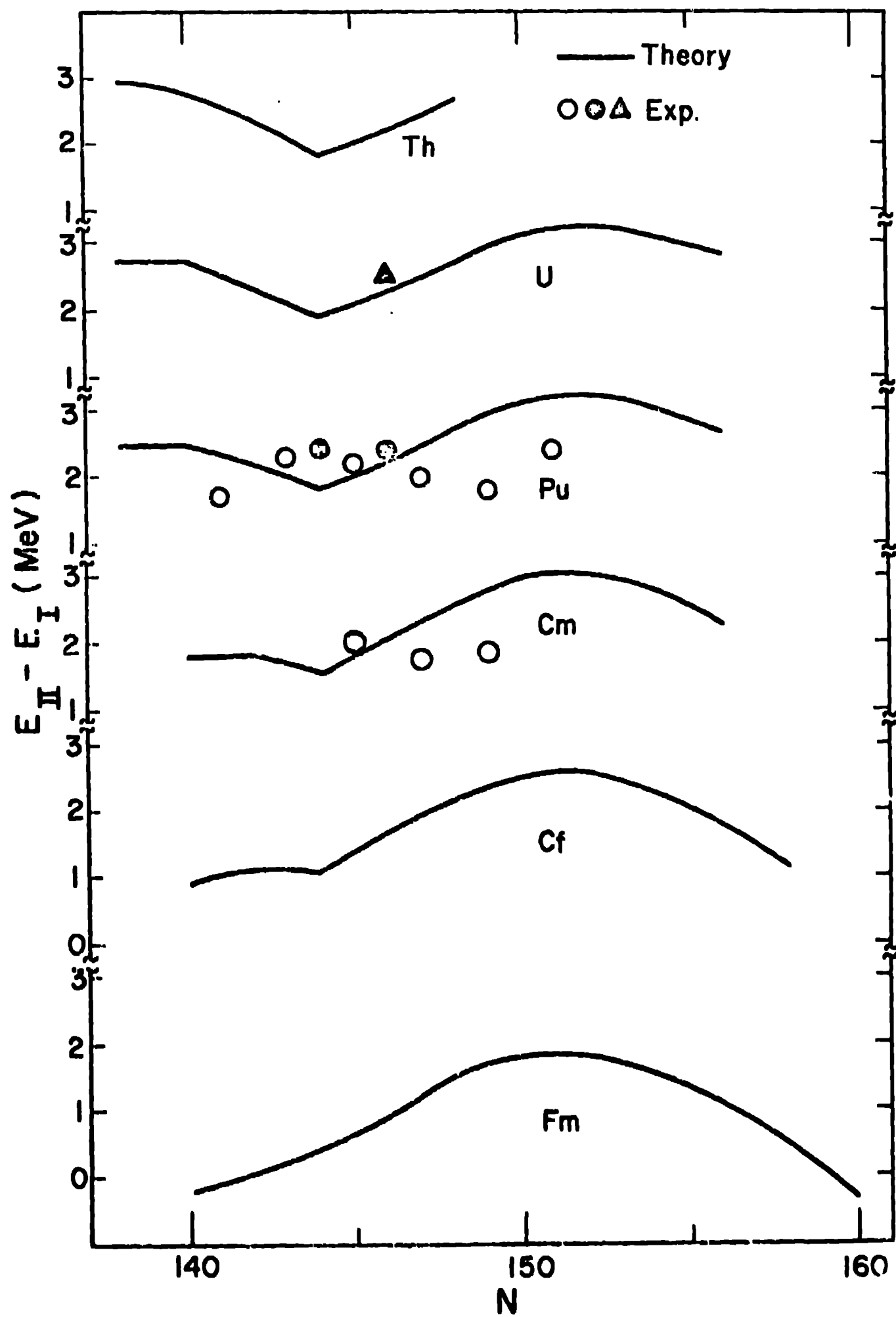


Figure 12

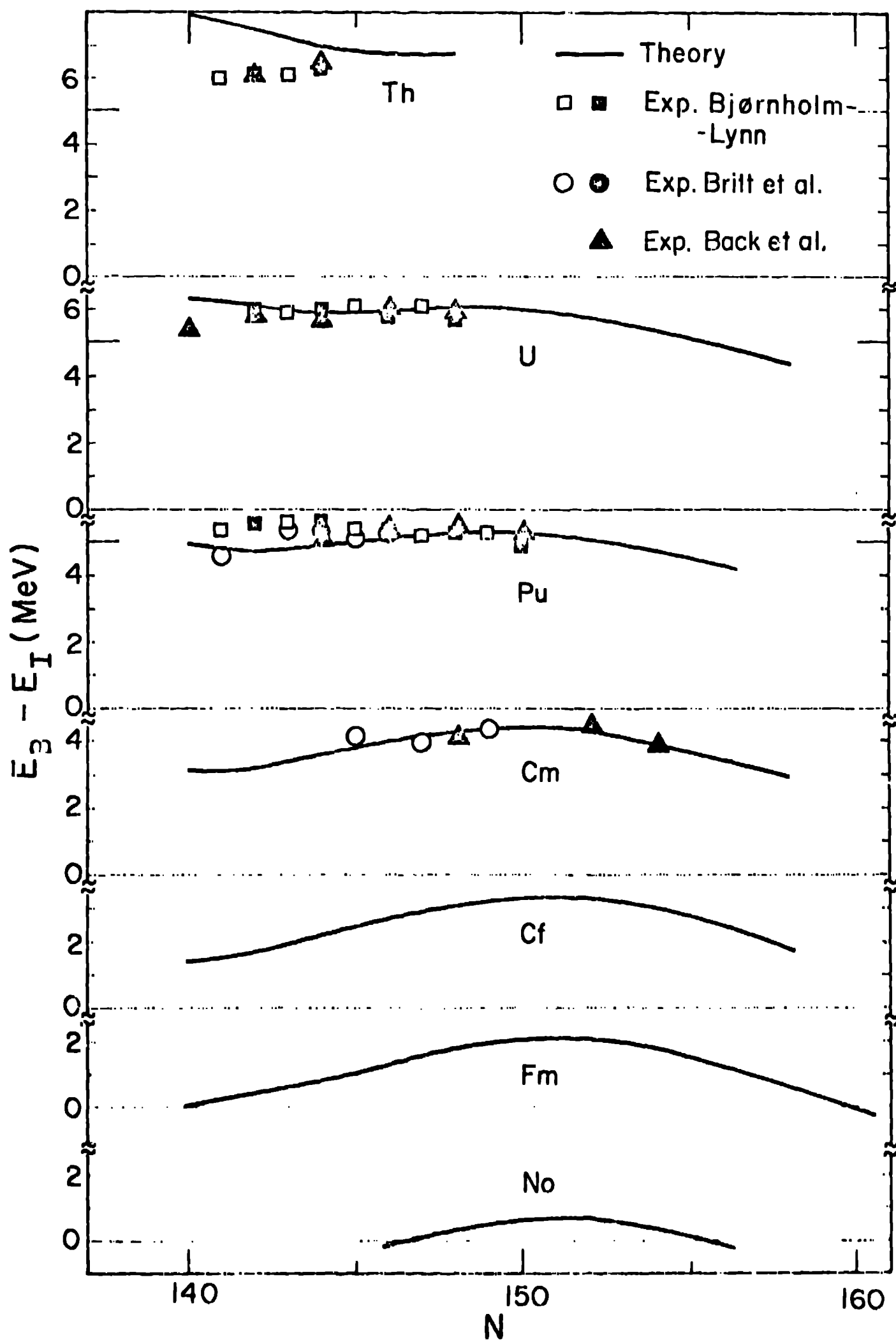


Figure 12

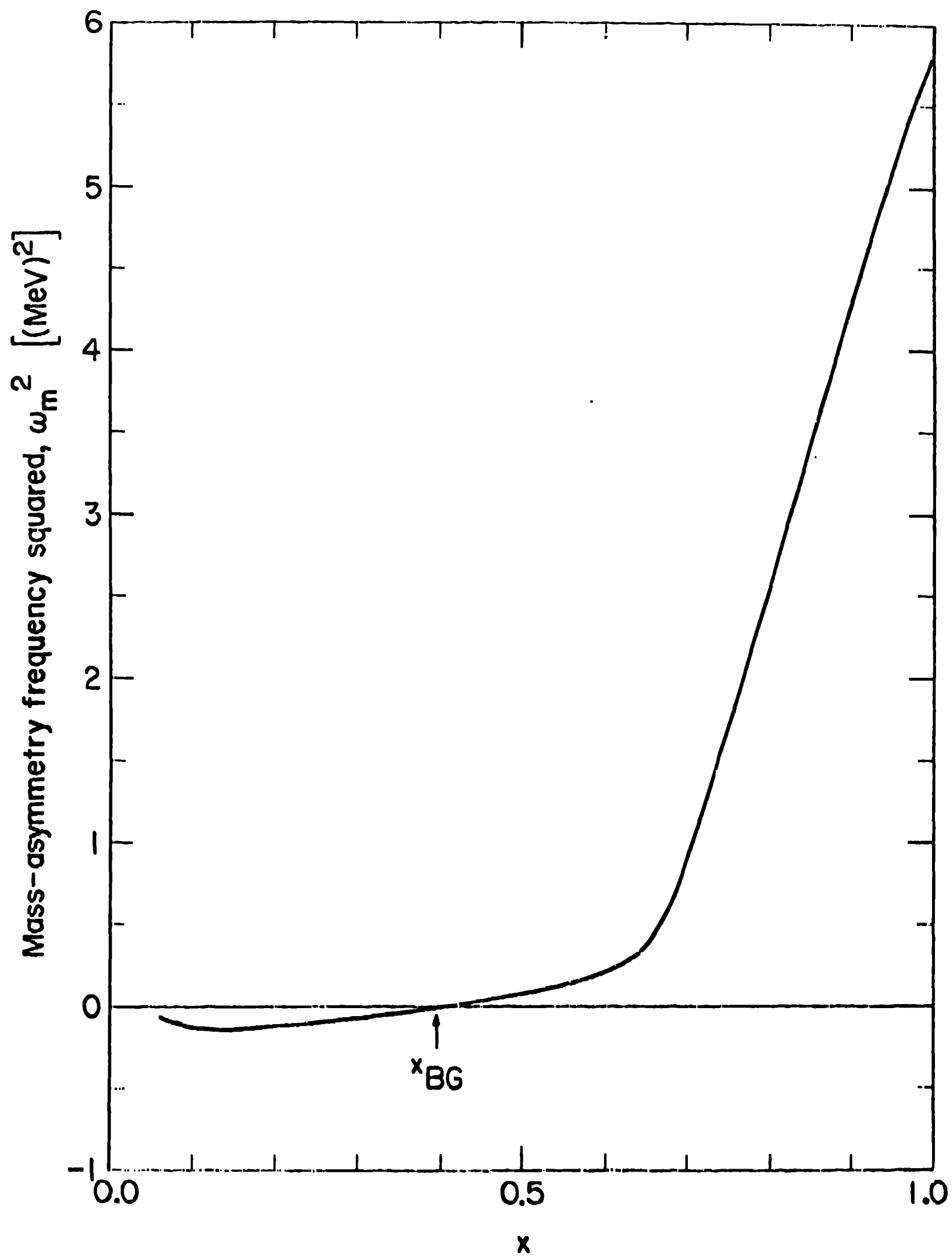


Figure 14

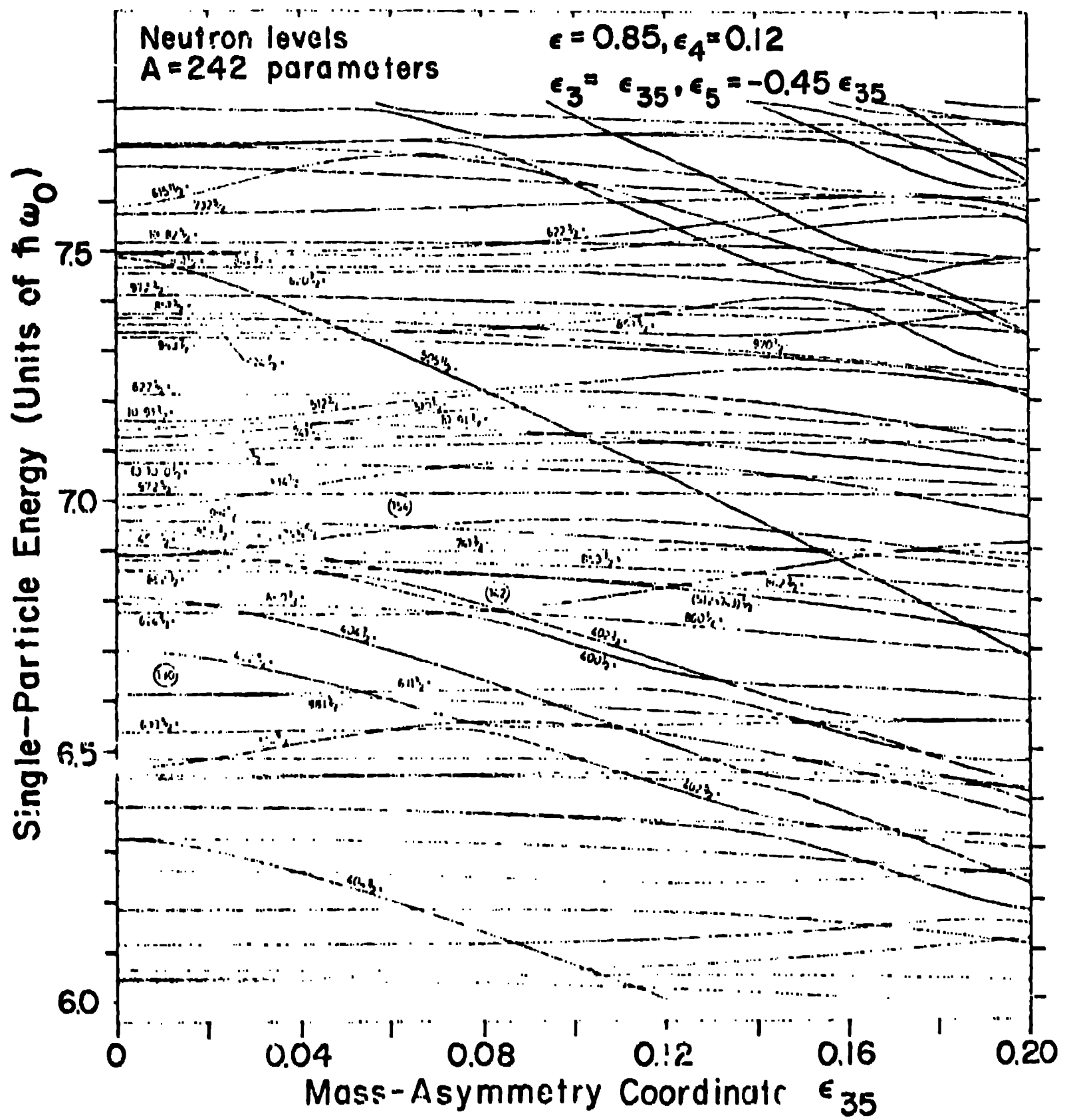


Figure 15

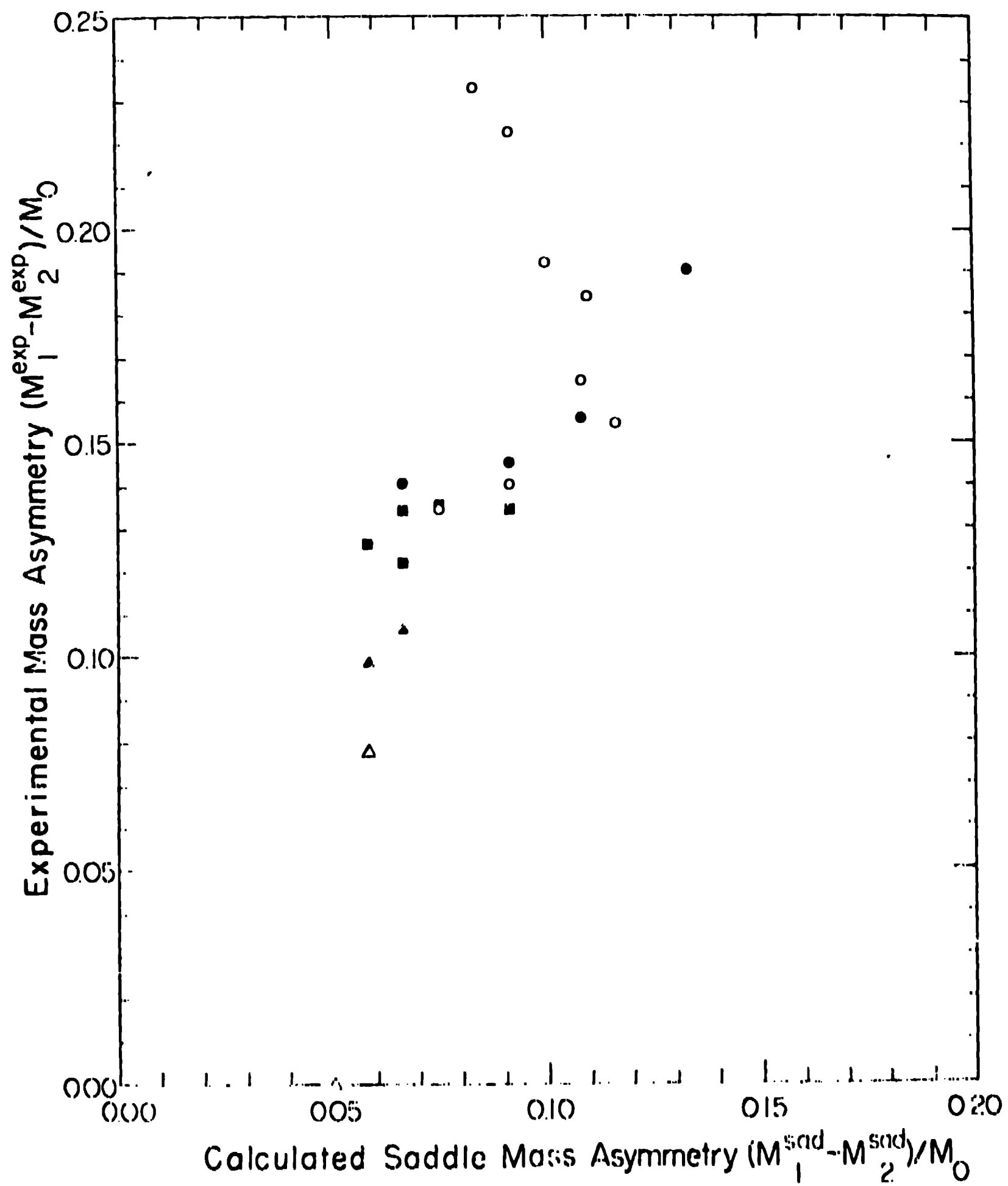


Figure 16



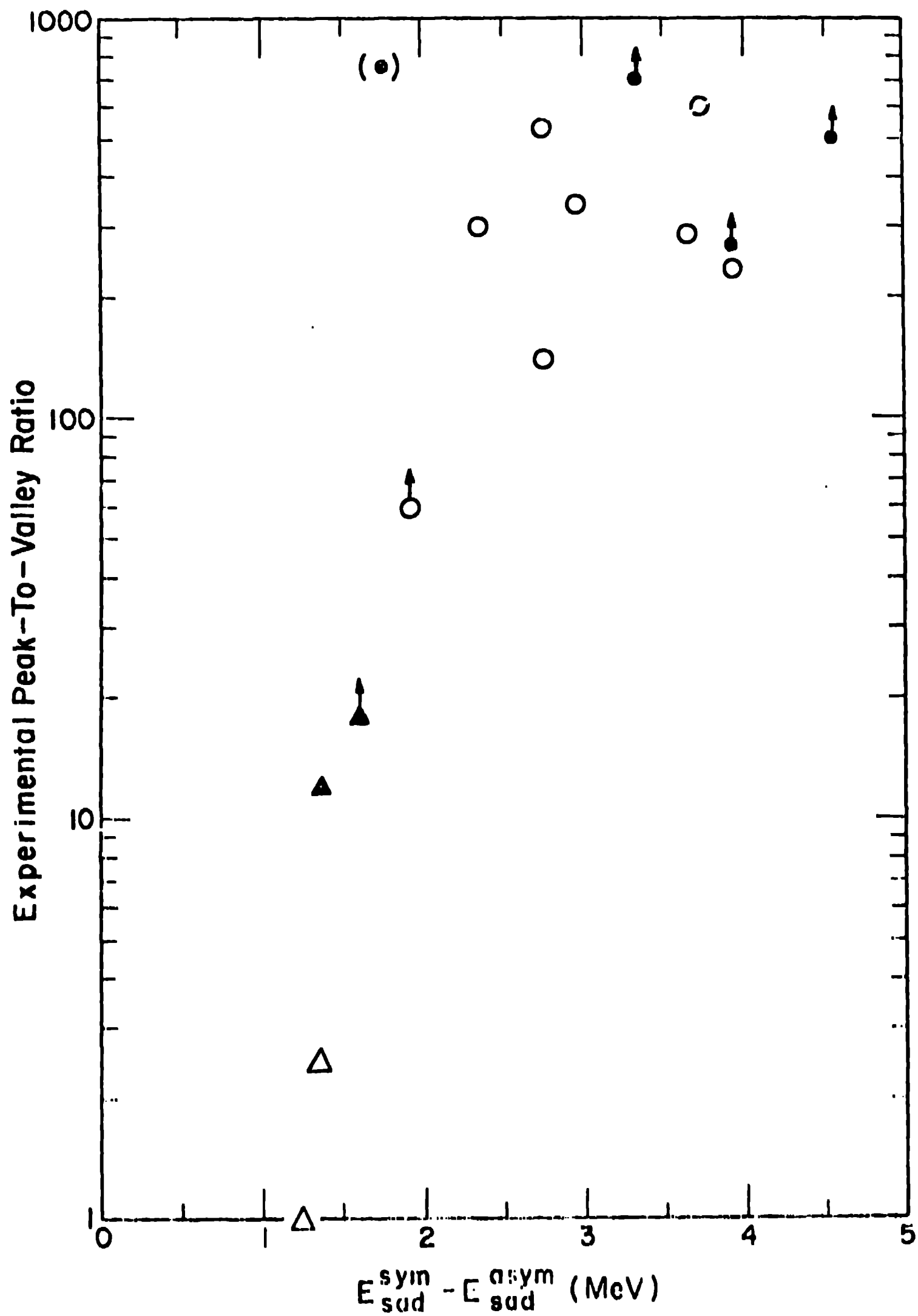


Figure 17

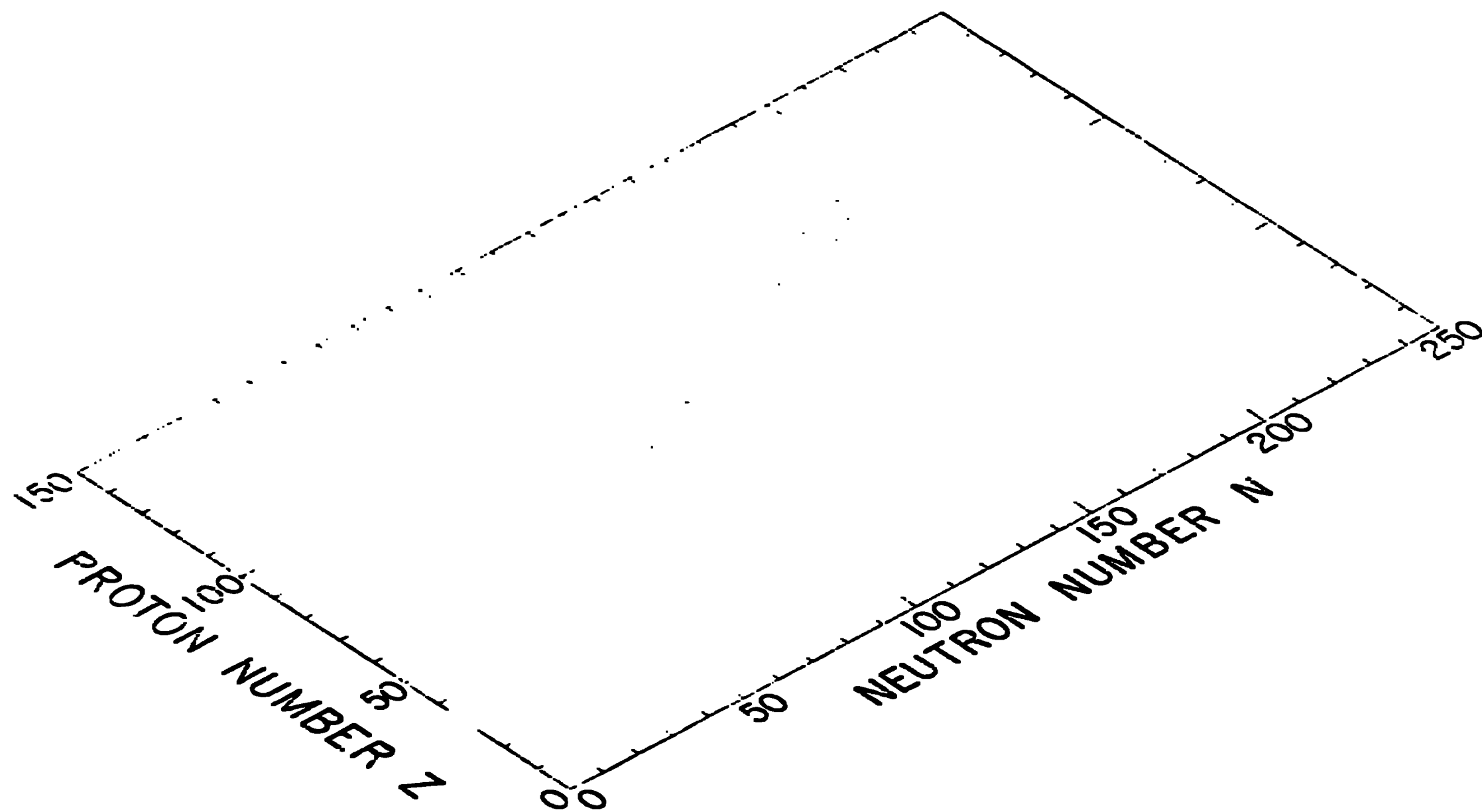


Figure 18